MNRAS 000, 1–24 (2025) Preprint 10 September 2026 Compiled using MNRAS LATEX style file v3.3

Planetary engulfment as a solution to solar-model discrepancies and its implications for planetary systems

Mutlu Yıldız[1]⋆ †
Department of Astronomy and Space Sciences, Faculty of Science, Ege University, 35100, İzmir, Turkey

Accepted XXX. Received YYY; in original form ZZZ

ABSTRACT

Thousands of close-in exoplanets suggest that planetary engulfment may be common during stellar evolution. We investigate whether early accretion of planetary material can resolve discrepancies between standard solar models and observations, including helioseismic sound-speed anomalies, the convection-zone depth, and surface abundances. Using MESA, we model pre-main-sequence accretion of metal-rich material representing planetary engulfment, followed by metal-poor disc accretion associated with planet formation. Model DD1020, combining planetary engulfment and turbulent mixing, provides the best agreement with helioseismic constraints. It favours a super-Earth of mass ~ 5.6 $M_\oplus$ (0.33 M_N) (Dev Dilek), while related best-fitting models favour $\sim$ 5–10 $M_\oplus$. The dissolved planetary material settles below the convection zone (m = 0.96–0.973 $M_\odot$), producing a localized heavy-element enhancement that modifies opacity and internal stratification. Optimized control models with variable mixing-length parameters and turbulent mixing but without engulfment improve the agreement only partially. Bayesian Information Criterion analysis shows that the improvement cannot be explained solely by increased model flexibility. The observed solar lithium depletion can be reproduced if the accreted material is lithium-poor and the engulfed planet has a mass of 4.6–5.8 $M_\oplus$. We also assess the physical feasibility of engulfment using Roche-lobe stability, pressure-dependent planetary structure models, and classical aerodynamic drag and ablation. A compact rocky planet can traverse the solar convective envelope with negligible mass loss, providing independent support for the proposed scenario.

Key words: Sun: helioseismology – Sun: interior – Sun: evolution – Sun: oscillation – planet–star interactions

1 INTRODUCTION

The Sun is, of course, one of the stars whose structure and evolution we know best. In order to understand stellar interiors, the fundamental stellar parameters, such as mass, radius, and luminosity, must be accurately determined from observations. In addition to the accurate determination of these parameters, the Sun offers two further major advantages. One of which is that its age is well determined, and the other is that three very important constraints for interior regions have been measured precisely with helioseismic methods. These constraints are the sound speed (c) almost from the center to the surface (Basu et al. 1997), the bottom radius ($R_{\rm bcz}$) of the convective zone (Basu & Antia 1997), and the surface helium ($Y_{\rm s}$) abundance (Basu & Antia 1995). A similar situation applies to the surface metallicity inferred from the solar spectrum (Asplund et al. (2009) - A09, Grevesse & Sauval (1998) - GS98). However, recent measurements by Magg et al. (2022) revealed that we need to approach this issue more carefully. We can also add neutrino fluxes to these constraints (Kunitomo, Guillot, & Buldgen 2022).

In the radiative region, opacity, which is very sensitive to the abundance of heavy elements, is one of the primary factors shaping the inner regions of stars. Many studies (Bahcall & Pinsonneault 2004; Guzik, Watson, & Cox 2005; Buldgen et al. 2025) have shown that the transition from a high-metallicity GS98 solar composition to a low-metallicity A09 solar composition also causes an increase in the relative sound speed difference between the Sun and solar model ($\delta c/c$) spike below the solar convective zone. However, this spike in general exists in all cases and however, the physical origin of this spike remains an open question.

How well do current solar models reproduce these observational constraints? Existing solar models generally exhibit the same systematic behaviour: beneath the convective envelope, the calculated sound speed is lower than the helioseismically inferred value, while the predicted $R_{\rm bcz}$ is larger than observed. The situation is a little different for the surface chemical composition. If $Y_{\rm s}$ is consistent with the observation, $Z_{\rm s}$ is inconsistent, and vice versa. Many alternative solar models have been made based on the effects of enhanced opacity, Ne abundance, diffusion coefficients, etc., to eliminate the difference in the sound speed. Considering the Sun as a planet host, solar models with mass accretion of material with low-Z (Castro, Vauclair, & Richard 2007; Guzik & Mussack 2010) and high-Z (Serenelli, Haxton, & Peña-Garay 2011; Zhang, Li, & Christensen-Dalsgaard 2019) are studied in detail. These studies show that pre-main-sequence (pre-MS) accretion (Hartmann, Herczeg, & Calvet 2016) significantly affects the structure of the solar models. The primary objective of this study is to construct solar models that simultaneously satisfy

⋆ E-mail: mutlu.yildiz@ege.edu.tr
† ORCID: 0000-0002-7772-7641

the available observational constraints by incorporating planetary engulfment within the framework of stellar evolution theory.

The discovery of planets in other star systems has profoundly and irreversibly changed our perception of the universe. Planetary statistics compiled in TEPCat show that close-in giant planets span a broad range of masses and orbital distances, with a representative hot-Jupiter population centred around $\sim$ 3 M_J and $\sim$ 0.06 AU from their host stars (Southworth 2011). Although hot Jupiters constitute only a small fraction of the known exoplanet population, they demonstrate that massive planets can migrate to very small orbital separations, where tidal interaction and eventual engulfment become possible. This implies that a hot giant gas planet may have been very close to its host star. Jupiter, the largest planet in the Solar System, is considerably farther from the Sun, $\sim$ 5 AU. The difference between systems can be evaluated to understand the evolution of protoplanetary disks during planet formation. This difference will also aid in understanding whether the Solar System and some similar systems may have engulfed their hot Jupiter, Neptune (Spina et al. 2015) or super-Earth (Martin & Livio 2016). The compositional contrast between the planetary and convective zone material and the location of dissolution are fundamental parameters for detecting the signature of the planetary engulfment.

The pronounced lithium depletion observed in the Sun remains a long-standing problem in stellar physics. Although the proto-solar nebula is inferred to have had a lithium abundance of A(Li)=3.3, consistent with meteoritic values, the present-day photospheric abundance is only A(Li)=1.1 (Grevesse & Sauval 1998), implying a depletion exceeding two orders of magnitude over the solar lifetime. A general expectation has therefore emerged that additional mixing processes operating below the convective boundary—such as convective overshoot, rotationally induced shear mixing, tachocline-driven turbulence, or internal gravity waves—transport lithium to deeper layers where it is efficiently destroyed by proton captures. The lithium content of planet-hosting stars has also been widely debated: some studies report enhanced lithium depletion in solar-type stars hosting close-in planets (e.g. Israelian et al. (2009); Ryabchikova et al. (2022)), based on lithium-poor stellar pairs), while others find no statistically significant difference compared to field stars (e.g. Ryan (2000)). In this context, addressing the lithium problem within the framework of non-standard solar and stellar models appears to be a particularly promising approach for understanding lithium evolution in solar-type stars.

Planetary migration is one of the central topics in studies of planetary-system evolution. For example, according to the Nice model (Desch 2007), gas giants were once much closer to the Sun, but over time they moved away to their current positions.

Astronomical events and the frequency of their occurrence can be elucidated by analyzing their effects on objects such as planets with solid structures. The Chicxulub impact on Earth is perhaps the best example of such a record (Morgan et al. 2022). Stars may also preserve signatures of major astrophysical events, provided that sufficiently accurate probes of their internal structures are available. Despite their gaseous nature, the unmixed or partly mixed layers of stars can also maintain a good chronological record of events and dates, as long as their effects can be determined. Helioseismic data for the Sun, especially the speed of sound, constitutes a very important potential for this recording. For example, for planetary engulfment to affect the host spectrum, the mass of the engulfed planet must be comparable to the total metallicity content of the host convective zone. Yana Galarza et al. (2024) find that the planet-hosting star TOI-1173 A in the wide binary system is enhanced in refractory elements such as iron by more than 0.05 dex, and suggest the engulfment of $\sim$18 $M_\oplus$ of rocky material in star A. The extent to which planetary engulfment affects the asteroseismic data of Sun-like oscillating stars should also be investigated.

Throughout this paper, we refer to the hypothetical engulfed hot Neptune-like planet or super-Earth as Dev Dilek[1]. This planetary-engulfment hypothesis provides the physical framework explored for improving solar models. The success of this approach depends on how consistent the solar models are with the Sun in terms of the speed of sound, the bottom radius of the convective zone, and the surface chemical composition.

Numerous studies in the literature examine the effects of self-pollution on element abundances using spectral data of planet hosts (Gonzalez 1997; Meléndez et al. 2009; Yun et al. 2024; Sun et al. 2025; Soares et al. 2025; Nordlund 2025). Planet formation in the disk itself consists of the processes of separation and possibly recombination of chemical elements. While the formation process continues in the disk structures, gas flows containing volatile elements are observed outward (Nordlund 2025). In the Sun, there is spectral evidence that refractory elements are depleted. Although there have been significant advances in the effects of self-pollution on the chemical element abundances of the host, whether it includes engulfment or not, however, the role of planetary engulfment in shaping stellar chemical abundances remains poorly understood. In the case of engulfment, the bulk of the planetary material is deposited below the outer convective envelope of the host, either by direct burial or by thermohaline mixing (Behmard et al. 2023; Soares et al. 2025; Winnick et al. 2025). A crucial factor in understanding the impact of planetary engulfment on the stellar spectrum is the variation in core and envelope chemical compositions, which depends on the characteristics of the engulfed planet. If the bulk metal content (abundance of heavy elements) of the planet and the star is similar or identical, an excess of refractory elements in the planetary core leads to an excess of volatile elements in the envelope. When such a planet is engulfed, very different signatures can appear in the stellar spectrum depending on which regions of the planet dissolve into which regions of the star. For example, if the planetary envelope, which is rich in volatile elements, dissolves into the star's convective zone, and the planetary core dissolves below the star's convective zone, a deficiency of refractory elements will be observed in the star's spectrum. Advances in this area are closely related to the increased precision of the chemical abundances calculated from the host spectrum.

Meléndez et al. (2009) first reported that the Sun's refractory elements are relatively depleted compared to volatile elements and suggested that depletion may be related to the presence of rocky planets. Yun et al. (2024) find that planet hosts with giant planets are more depleted in refractory elements than those with rocky planets. They also state that sub-Jovian hosts demonstrate more depleted refractory trends than stars hosting Jovian-mass planets. However, Bedell et al. (2018) recognize that some of the depletion trend may be primarily caused by Galactic chemical evolution.

Soares et al. (2025) find an engulfment rate no higher than 20% for Sun-like stars that may reveal detectable traces of planet engulfment. For engulfment to create measurable signatures on the star's chemical composition, specific conditions are required. These include the total mass of the engulfed planet, the mass of the host's convective envelope, and the time elapsed over the engulfment.

[1] We refer to the hypothetical super-Mercury-like planet as Dev Dilek ("Great Wish"). The name is motivated by the historical and cultural association of Mercury with the Turkish name Dilek, traditionally associated with wishes directed toward Mercury. The prefix "Dev" means "giant" in Turkish.

Tidal interactions affect the evolution of close-in star–planet systems. Several events may have occurred due to planet engulfment (Hon et al. 2023; Rao et al. 2021; Lazovik 2023). These systems or events are known as V838 Mon (Retter et al. 2006), ASASSN-15qi (Herczeg et al. 2016), ASASSN-13db (Kashi, Michaelis, & Feigin 2019), and ZTF SLRN-2020 (De et al. 2023). The infrared emission from ZTF SLRN-2020 confirmed that a main-sequence (MS) or early subgiant branch star with a mass around 0.8 - 1.5 $M_{\odot}$ engulfed a planet, possibly culminating in the tide-induced orbital decay (De et al. 2023). The transient V838 Mon was formed by the engulfment of giant planets. As a planet's orbital speed decreases in the star's atmosphere, its kinetic energy is converted into heat, triggering deuterium fusion due to increasing temperature. The expanding envelope of the star results in the engulfment of two other planets. The 2014–2017 eruption of ASASSN-13db can result from the accretion of a protoplanet of a few Earth masses.

Direct observational evidence of changes in planetary transit periods facilitates the understanding of planetary engulfment, and a significant amount of this evidence exists. Such shifts have been observed for WASP-12b (Yee et al. 2020), HAT-P-19 b, and Kepler-1658b (Vissapragada et al. 2022; Jackson, Adams, & Morgenthaler 2023). Moreover, older hot Jupiters are farther from the host star, whereas the younger ones are closer (Jackson, Barnes, & Greenberg 2009). The younger hot Jupiters must have thus been engulfed over time due to the tidal effect (Ronco et al. 2020).

An interesting feature of the Solar System, different from other planetary systems, is the absence of a super-Earth in our system. Martin & Livio (2016) explains this lack of a super-Earth by considering turbulence in a protoplanetary system. A dead zone (a region of low turbulence) can contain a lot of material in the inner parts of the disk, possibly allowing in situ formation. In fully turbulent disks, however, there is insufficient material for in situ formation. In such a case, super-Earths form far away in the disk and migrate inward. Both of these mechanisms can be effective in planetary systems. According to Martin & Livio (2016), the super-Earths could migrate through the gas disk and fall into the Sun.

The standard theory of stellar evolution explains that nuclear reactions, diffusion, and convection influence the chemical composition from the center to the surface of the Sun and similar stars. The mass exchange of stars during the early or late stages of evolution also affects their surface chemical composition (Church, Mustill, & Liu 2020; Nagar, Spina, & Karakas 2020). Chemical evidence for planetary ingestion is found in about one-fourth of Sun-like stars in binary systems (Spina et al. 2021; Ong et al. 2024).

The structural differences between solar models and the Sun can stem from various influences. It is necessary to test whether these influences are alternatives to planetary engulfment. In this study, we tested each of the following influences: opacity, the equation of state (EOS), turbulent mixing, thermohaline mixing, and various mixing-length theory (MLT) parameterizations, and evaluated their potential as alternatives to planetary engulfment (see Section 4).

The remainder of this paper is organized as follows. The modeling methods and the computation method of the mass of the engulfed planet from the non-standard models are described in Section 2. Section 3 is for the effect of mass exchange on the chemical composition of host stars. Section 4 presents and discusses the results. Finally, Section 5 discusses the astrophysical implications of the engulfment scenario, while Section 6 presents an order-of-magnitude analysis of the physical feasibility of transporting planetary material to the base of the solar convection zone. Finally, Section 7 summarizes our main conclusions.

2 PECULARITIES IN THE CHEMICAL COMPOSITION OF THE SUN

2.1 Chemical composition of the Sun in comparison with the solar twins and solar-like stars

Numerous studies have shown that the chemical composition of the Sun differs from that of solar twins and solar-like stars. The most prominent difference is the relative depletion of refractory elements with respect to volatile elements. Since these two groups of elements have markedly different condensation temperatures, this abundance pattern has frequently been interpreted as evidence of self-pollution associated with the chemical segregation of solids and gas during the planet-formation process.

Planets are considerably richer in heavy elements than stars. Rocky planets, as well as the cores of giant planets, are composed predominantly of refractory material, whereas the envelopes of giant planets are expected to be relatively enriched in volatile elements. From this perspective, the depletion of refractory elements observed in the solar photosphere can be explained if the volatile-rich envelope of an engulfed planet is mixed into the solar convective envelope. In contrast, the planetary core may survive the dissolution of the envelope and continue sinking into deeper stellar layers before dissolving.

2.2 Effect of mass exchange on the chemical composition of host stars

Mass exchange during stellar evolution remains an important issue in understanding stellar structure and chemical evolution. In most stellar evolution calculations, however, it is generally assumed that mass accretion ends at a very early stage and that stars subsequently evolve at nearly constant mass. This assumption is widely adopted for low-mass stars. However, significant mass exchange between the protoplanetary disk and the central star has been reported (Beccari et al. 2015; Hartigan, Edwards, & Ghandour 1995; Ray & Ferreira 2021), potentially affecting both the angular momentum and the chemical composition of the star. Although the effects on angular momentum are largely erased by subsequent angular-momentum loss, the chemical signatures of such accretion episodes may persist, particularly in the outer stellar layers.

Protoplanetary disks are highly dynamic environments; moreover, dense matter exchange possibly occurs between the proto-star and its environment. While planets are composed predominantly of heavy elements, some of the metal-poor gas remaining in the disk may accrete onto the star. This causes the convective envelope of the star to differ from the deep inner layers. The difference in chemical compositions depends on the amount of accreted gas and the total mass of the convective envelope; the thinner the convective envelope, the greater the difference.

If a planet composed primarily of heavy elements, such as Uranus or Neptune (81 and 85 percent of total mass (Yıldız et al. 2024), respectively), is engulfed due to orbital instability or tidal interaction (Kane 2023; Ronco et al. 2020), the burial continues until the mean planet density equals the local density of the star or until the planet fills its Roche lobe (Behmard et al. 2023; O'Connor et al. 2023). If the burial is sufficiently rapid, the planet, at least its core, will not erode substantially. If density equalization occurs within the convective envelope, the planet dissolves and mixes with the outer envelope. If the planet falls below the convective zone, a local increase in metallicity occurs where it dissolves. The difference in the speed of sound between the Sun and its model agrees well with this scenario.

The interaction between an engulfed planet and the stellar envelope is expected to involve a range of complex physical processes, including planetary layering, ablation, ram-pressure stripping, shock heating, and tidal deformation. These processes can result in partial, rather than complete, dissolution of the planet, with different planetary layers being deposited at different depths within the stellar envelope. Recent hydrodynamical studies have demonstrated that such partial dissolution scenarios are physically plausible and can lead to selective mixing of planetary material, without requiring the full disruption of the planetary core (e.g. Yarza et al. (2023); Lau et al. (2025)). A detailed hydrodynamical treatment of these processes is beyond the scope of the present work and is deferred to future studies.

The preferred interior models of Jupiter, Saturn, Uranus, and Neptune (Yıldız et al. 2024) are used to determine the minimum value for the total metallicity of the proto-solar disk: 0.314 M_J. If this mass is considered the mass of dust in the disk and a standard dust-to-gas mass ratio (Rilinger et al. 2023) of 0.01 is assumed, the minimum mass of the proto-solar disk will be 31.4 M_J = 0.030 $M_\odot$. The mass of the present solar convective envelope is approximately 0.02-0.03 $M_\odot$ (Christensen-Dalsgaard et al. 1996) and comparable to that of the proto-solar disk. The mass of the solar outer regions may be the accreted mass from the dust-free or dust-deficient gas of the proto-solar disk. Accretion of material with a composition modified by planet formation may also help reconcile solar models with the observed solar neutrino constraints. Kunitomo, Guillot, & Buldgen (2022) show that inhomogeneous solar models, where the outer 4 percent of the total mass is metal-poor, are much more compatible with neutrino constraints, and their models constructed with homogeneous and metal-poor accretions yield solar models within 2.7 and 1.3 σ of all neutrino constraints, respectively.

3 METHODS

3.1 Standard Solar Models

Standard solar models are constructed by numerically solving the four stellar structure equations using the finite-difference method on an adaptive mesh extending from the solar center to the surface. To determine the solution for a given mass and chemical composition, EOS, nuclear reactions, and opacity must be calculated. We construct solar models using the ANKİ and MESA codes to see how the model structure depends on the codes. The ANKİ and MESA codes provide opacity from OPAL tables (Iglesias & Rogers 1996). The MESA code uses either FreeEOS (Irwin 2012) or OPAL EOS (Rogers & Nayfonov 2002) for determining the EOS, and the ANKİ code has its own EOS routines and solves the Saha equation (Yıldız & Kızıloğlu 1997). The ANKİ code considers nuclear reaction rates derived by Angulo et al. (1999) and Caughlan & Fowler (1988), and the MESA code uses the updated rates (Kunz et al. 2002; Cyburt et al. 2010). The microscopic diffusion of chemical elements in the ANKİ and MESA codes is computed using the methods proposed by Thoul, Bahcall, & Loeb (1994) and Paquette et al. (1986), respectively. Both these codes treat convection using the standard MLT (Böhm-Vitense 1958).

3.2 Non-Standard Solar Models with variable mass

Planet formation in the disk leads to the separation of heavy elements from hydrogen and helium, and the chemical separation of heavy elements into volatile and refractory elements, depending on their location in the disk. Taking this chemical separation into account, the solar surface composition can be resolved by creating low-Z accretion solar models (Castro, Vauclair, & Richard 2007; Guzik & Mussack 2010). Serenelli, Haxton, & Peña-Garay (2011) and Zhang, Li, & Christensen-Dalsgaard (2019) consider various types of accretion, including high-Z materials. These studies improve some properties of solar models.

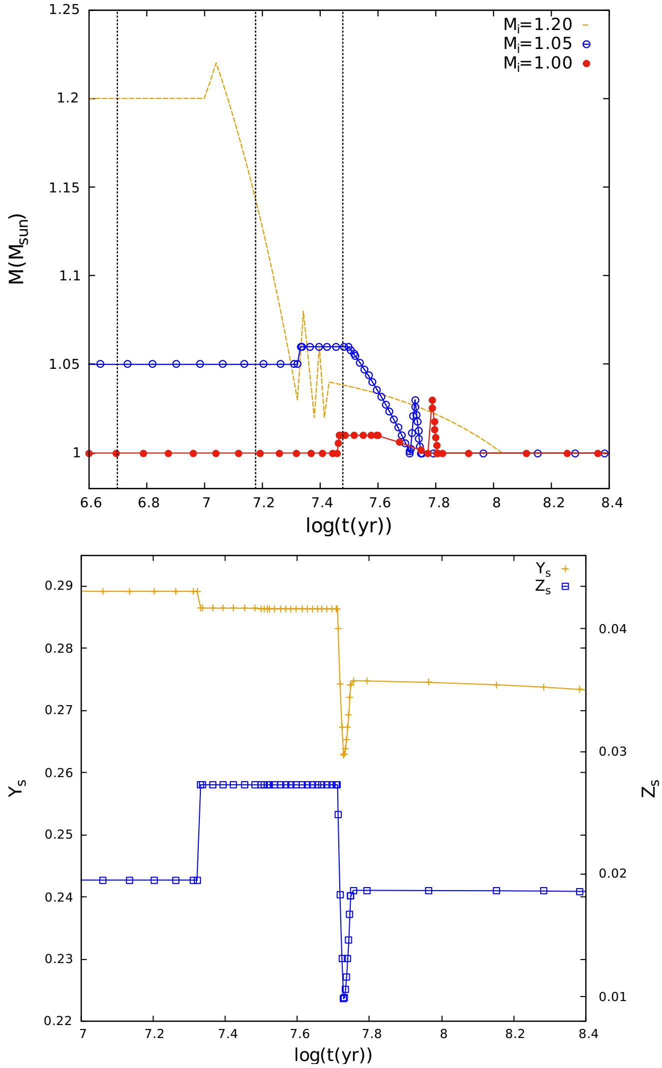

Figure 1. Change in the mass and surface composition of Model NCz195 (see Section 4.3) with time. (*a*) Mass is plotted with respect to time for the models with M_i = 1.2 (Model N), 1.05 (Model NCz195), and 1.00 $M_\odot$ (Model NCz198). The mass of Model NCz198 changes in between $\log(t(yr))$ = 7.46 and 7.8. The vertical dotted lines show the starting times of early (3 Myr), intermediate (15 Myr), and late (30 Myr) representative accretions used by Serenelli, Haxton, & Peña-Garay (2011). (*b*) Y_s and Z_s of Model NCz195 are plotted with respect to age in pre-MS phase. Initial Y_s and Z_s are 0.2892 and 0.0195, respectively. After two mass accretions and mass losses, Y_s and Z_s are about 0.275 and 0.0187 at about 57 Myr, respectively.

We construct non-standard solar models using the MESA code, using losing and accreting mass with different chemical compositions. The MESA version is v15140. This version changes mass using choice `mass_change`. If `mass_change` is positive, then the mass is accreted. If `mass_change` is negative, then the mass is lost. The chemical composition of the accreted material is specified through the `accretion_h1` and `accretion_he4` parameters. The first parameter is used for hydrogen (X) and the other for helium abundance (Y). The $1 - X - Y$ difference gives the metallicity (Z). By accreting and losing mass several times, a metallicity profile of the outer regions of solar models is obtained so that the difference in the speed of sound between the model and the Sun is considerably reduced. Moreover, the surface chemical composition of models will agree with the observed values. Figure 1a shows the changes in mass in the early phase of the three models (Model N, NCz195, and NCz198, see Section 4.3) with different initial masses (M_i). For Model N, the mass transfer begins at about 10^7 yr and ends at about 10^8 yr. The initial mass is 1.2 $\mathrm{M}_\odot$, and the mass varies eight times. M_i of Model NCz195 and NCz198 is 1.05 and 1.00 $\mathrm{M}_\odot$, respectively. These models accrete mass twice. The first one is the accretion of metal-rich material, while the second one is the accretion of low-Z material. In Figure 1b, Y_s and Z_s of Model NCz195 are plotted with respect to $\log(t)$. The initial values of Y_s and Z_s are 0.2892 and 0.0195, respectively. At 57 Myr, $Y_\mathrm{s} = 0.275$ and $Z_\mathrm{s} = 0.0187$. For the current Sun, these values are reduced to $Y_\mathrm{s} = 0.2485$ and $Z_\mathrm{s} = 0.0167$ due to microscopic diffusion (see Table 2).

The initial sequence of models was not intended to reproduce a physically realistic accretion history. Instead, its purpose was to determine the chemical composition profile required to reconcile solar models with the observational constraints. What we do is essentially to obtain the appropriate chemical composition profile that will eliminate the differences between the solar models and the Sun. We obtain this profile by applying mass accretion with low-Z and high-Z and mass-loss. Later, considering the minimum mass of the protosolar disk (0.030 $\mathrm{M}_\odot$) and applying only two accretions (no mass-loss), models with M_i=0.97 $\mathrm{M}_\odot$ are constructed with a more realistic approach (see Section 4.15).

These models have two mass accretions in the early stage. The first one includes metal-rich gas and may represent planet engulfment. As a result of planet formation in the disk, chemical elements separate from each other in various ways. Since planets are mostly, if not entirely, composed of metal, we should also talk about a metal-poor gas in the disk. The second mass accretion represents the flow of this metal-poor gas to the star.

The mass exchange process complicates to calibrate the model to the observation. In the models we make, especially in the layer below the convective zone, the steep chemical composition gradient makes it difficult to fine-tune the convective zone base radius. For this reason, we need to make many solar models. In our first models (Model N), we set the M_i quite high to facilitate chemical stratification and applied mass accretion four times. By carefully choosing the accretion timings and applying fewer accretions, we were able to obtain solar models with smaller M_i (Model NCz198, for example).

For solar models with high M_i, the mixing-length parameter (α) is constant during solar evolution. For models with low M_i, α is initially kept at a lower value in the early phase of evolution and is increased to a higher value to calibrate the radius of the models to the present radius (see Section 4.11 and 4.14). We also test the effect of constant and variable MLT parameter during the solar evolution.

Various effects, as well as different MLT parameterizations, are tested for their ability to improve solar models. The main effects available in the MESA code are opacity (see Section 4.9), EOS (see Section 4.10), turbulent mixing (see Section 4.12), and thermohaline mixing (see Section 4.13). While investigating the opacity effect, we are also testing different solar abundance mixtures. We also consider the combined impact of planet engulfment and turbulent mixing in Sections 4.14 and 4.15.

3.3 Integration for the excess total metallicity in non-standard solar models

The mass of the dissolved planet is calculated from the metallicity excess below the convective zone in the solar model. To compute the metallicity excess, we numerically integrate $(Z - Z_0)dm$ using the mesh points that are sufficiently frequent below the convective zone. Let $y = (Z - Z_0)$. At the ith point, the value of y is y_i. The area $y\ dm$ between the interval m_i and m_{i+1} can be approximately computed by multiplying the mean value of y_i and y_{i+1} and $dm = m_{i+1} - m_i$. Then, the total metallicity excess in the relevant mass interval is computed from

$$M_\mathrm{z} = \int_{M_1}^{M_2} (Z - Z_0)dm = \sum \frac{y_i + y_{i+1}}{2}(m_{i+1} - m_i). \quad (1)$$

4 SOLAR MODELS AND RESULTS

4.1 Standard solar models

To test whether planet engulfment makes the solar model more compatible with the observational data of the Sun, we obtained solar models using two different codes, namely ANKİ (Ezer & Cameron 1965; Yıldız et al. 2014; Yıldız, Çelik Orhan, & Kayhan 2015; Yıldız 2015) and MESA (Paxton et al. 2011) codes.

As a reference for the subsequent non-standard models, we first construct standard solar models using the ANKİ (Ezer & Cameron 1965; Yıldız et al. 2014; Yıldız, Çelik Orhan, & Kayhan 2015; Yıldız 2015) and MESA (Paxton et al. 2011) stellar evolution codes. Comparing these models allows us to evaluate the code dependence of the sound-speed profile before introducing planetary engulfment. The MESA code is used to reduce the difference between the model and the observational speed of sound by changing the abundance of heavy elements and helium under the convective zone in the model.

Owing to their high precision, helioseismic data are used to test the quality of solar models. In particular, the speed of sound provides one of the most stringent diagnostics of the difference between solar models and the Sun (Basu et al. 1997), over nearly the entire solar interior. Figure 2a and 2b plot the relative sound speed difference between the Sun and the solar models against the relative radius. The difference in the speed of sound is the highest at about r = 0.67 $\mathrm{R}_\odot$ below the convective zone for all models, particularly under the convective zone. In Figure 2a, the level of difference depends substantially on the initial metallicity of the model (Z_0). The difference decreases as the metallicity increases. Increasing Z_0 reduces the sound-speed discrepancy below the convective zone, but simultaneously leads to a surface metallicity significantly exceeding the observed value (Table 1). Z_s and Y_s of the ANKİ model agree well with the observed values. Z_s of the MESA model with $Z_0 = 0.015$ is almost the same as the observed value. However, for model fitting and observational Y_s, Z_0 must be around 0.0176.

The Z_0 of the ANKİ model is 0.0172. The Z_s and Y_s of this model agree more with the observed value of A09 but less with the (Magg et al. 2022) value, compared to the MESA model obtained for the same Z_0. The difference between the two models may stem from the different methods for the diffusion computations of the codes. This difference is most likely related to why the ANKİ model is more consistent with the observed sound speed (Figure 2a) in the solar core (r <0.3 $\mathrm{R}_\odot$). However, the MESA model with the same Z_0 is in better agreement with the Sun than the ANKİ model below the CZ.

Despite quantitative differences between the two evolution codes, both predict the same qualitative behaviour. These include the maximum sound speed difference being just below the convective zone

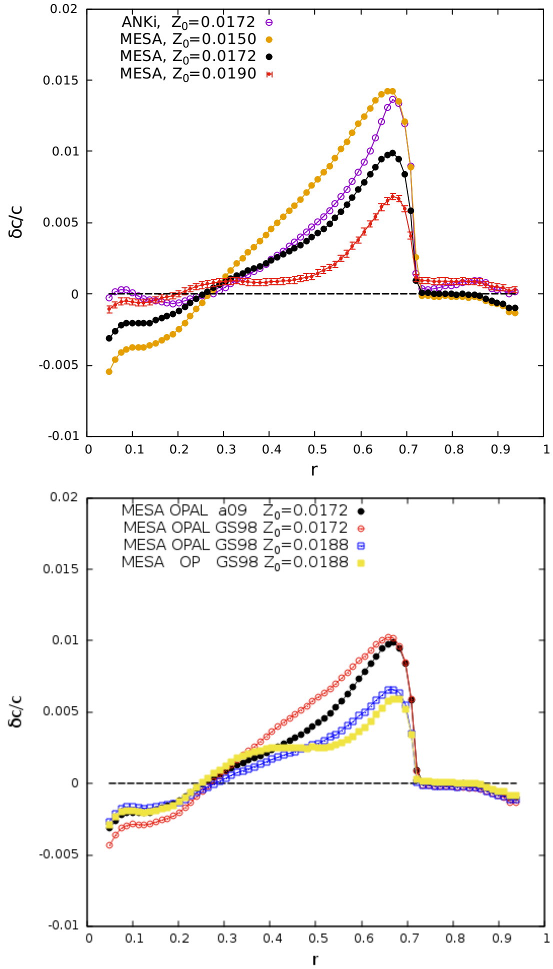

Figure 2. a) The sound speed difference between the Sun and the standard solar models constructed using the MESA and ANKİ codes. The MESA models have different metallicities (Z_0 = 0.015, Z_0 = 0.0172, and 0.0190). The largest sound-speed discrepancy occurs at r = 0.67R$_\odot$ for all models. Z_0 of the ANKİ model is 0.0172. b) ($\delta c/c$) is plotted for the solar models with Z_0 = 0.0172 but with the GS98 mixture (circle). The model with the same solar heavy element mixture but Z_0 = 0.0188 is represented with the square. This is the Z_0 of the model BP04 of Bahcall & Pinsonneault (2004). The filled squares show the solar model with the same Z_0 but with the OP opacity (Seaton 2005).

and the model sound speed increasing in the region r > 0.3 R$_\odot$ and decreasing in the region r < 0.3 R$_\odot$ as Z_0 increases.

The MESA models in Figure 2a are obtained using the OPAL opacity tables for the A09 mixture. Figure 2b plots the model obtained with the OPAL opacity tables for Z=0.0172, but for the GS98 mixture (`kap_file_prefix = 'gs98'`). The change in heavy-element mixture has only a modest effect on $(\delta c/c)_{\rm max}$. However, in deeper layers, especially in the layer between 0.4 and 0.65 R$_\odot$, the different mixtures have a limited effect on $\delta c/c$. This plot also shows a model with Z=0.0188 as a counterpart to the BP04 model obtained in Bahcall & Pinsonneault (2004). For this model, $(\delta c/c)_{\rm max}$ drops to 0.0066 (Table 1). The $\delta c/c$ profile of BP04 with this model is very similar, although the $(\delta c/c)_{\rm max}$ value of BP04 is slightly lower (0.004). We notice that $Y_{\rm s}$ of the models with Z=0.0188 is about 0.0043-0.0055 less than the observed value.

Table 1. Basic properties of the standard solar models with different metallicities, opacities, and mixtures constructed using MESA code. The observed values for the surface composition of the Sun are also given (Basu & Antia 1995; Asplund et al. 2009; Magg et al. 2022). For comparison, we also give the model constructed using ANKİ and the model BP04 of Bahcall & Pinsonneault (2004).

Code	Opac.	Mixt.	Z_0	Y_0	$Z_{\rm s}$	$Y_{\rm s}$	$(\delta c/c)_{\rm max}$
MESA	OPAL	A09	0.0150	0.2607	0.0135	0.2325	0.0145
MESA	OPAL	A09	0.0172	0.2742	0.0156	0.2458	0.0094
ANKİ	OPAL	A09	0.0172	0.2804	0.0134	0.2503	0.0140
MESA	OPAL	A09	0.0190	0.2854	0.0173	0.2569	0.0064
Obs.	——	——	——	——	0.0134	0.2485	—–
Unc.	——	——	——	——	0.0002	0.0034	—–
MESA	OPAL	GS98	0.0172	0.2622	0.0156	0.2348	0.0102
MESA	OPAL	GS98	0.0188	0.2717	0.0171	0.2442	0.0066
MESA	OP	GS98	0.0188	0.2670	0.0171	0.2428	0.0059
BP04	OPAL	GS98	0.0188	0.2736	0.0170	0.2430	0.0040
Obs.	——	——	——	——	0.0165	0.2485	—–
Unc.	——	——	——	——	0.0010	0.0034	—–

The solar model obtained with the same mixture (GS98) and the same Z (0.0188) but using OP opacity (Seaton 2005) tables (`kap_file_prefix = 'OP_gs98'`) is also plotted in Figure 2b. Although the two opacity tables show a very similar variation for $\delta c/c$, the $\delta c/c$ of the model obtained with the OP tables remains virtually constant in the region r=0.3-0.55 R$_\odot$.

Solar models and the Sun can agree well through opacity enhancements as a function of temperature alone (Bahcall, Serenelli, & Pinsonneault 2004; Buldgen et al. 2025) or density and temperature together (Yıldız 2011). It seems unlikely that this issue will be clarified anytime soon unless a new opacity more comprehensive than the OPAL (Iglesias & Rogers 1996) opacity is calculated.

4.2 How deep can an engulfed massive planet be buried?

The mean densities of early Jupiter and Neptune are approximately the same as the density just beneath the solar convection zone (Figure 3); this finding supports the proposed approach. When a planet enters the atmosphere of the star, it is buried under gravity, centrifugal, and drag forces (Behmard et al. 2023). Hydrodynamical calculations suggest that an engulfed planet may continue sinking through the stellar convective envelope under the combined effects of gravity, drag, and tidal interactions (Behmard et al. 2023). As the planet sinks, some of its outer layers erode, and the core of the planet probably survives. The mean density of the remaining part of the star-planet is similar to the density below the base of the convective zone of the star, during which the burial of the planet stops or the burial rate considerably decreases. Then, the planet dissolves after a certain time, depending on various interactions between the planet and the Sun. If a sufficiently compact remnant survives, it may dissolve below the convective-zone base, producing a localized enhancement in heavy-element abundance.

The highest mean density is observed for planets with a mass of 10 M$_\oplus$, approximately 10 g/cm^3; the central density of high-mass planets is similar to or higher than this value. Real planets are internally stratified, and different layers of an engulfed planet dissolve to varying depths of its host, depending on the local pressure-temperature-density profile of both the planet and the star. If the envelope of the engulfed planet dissolves and only the core remains, burial continues until $\rho_{\rm core} = \rho(r)$. In this case, if it is not completely eroded and dispersed, the residual concentration can decrease to r = 0.53 R$_\odot$

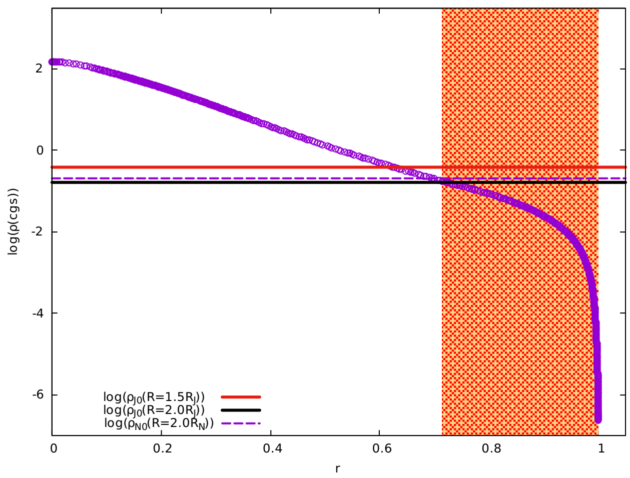

Figure 3. The density profile is plotted for the interior of the Sun. The horizontal lines show the mean density of young jovian planets with 1.5 R_J and 2.0 R_J. These values for planetary radius are suitable for young and highly irradiated hot gas giants.

(Behmard et al. 2023). The physical conditions under which ram pressure, tidal disruption, and Roche-lobe overflow become important are examined quantitatively in Section 6.

The internal structures and core properties of giant planets remain highly uncertain, even in the Solar System, with Jupiter's core mass and degree of mixing still under debate. Interior models of exoplanets similarly exhibit substantial degeneracies in core mass, composition, and thermal state. Accordingly, the core masses adopted for the engulfment candidates in this work should be regarded as order-of-magnitude estimates rather than precise values, and these uncertainties necessarily propagate into the predicted post-engulfment evolution. In particular, under the extreme temperature and pressure conditions encountered within stellar interiors, partially mixed or compositionally heterogeneous cores may experience erosion, partial dissolution, or destabilization following envelope stripping, potentially limiting long-term intact survival. Our analysis, therefore, does not assume universal core preservation but instead explores the conditions under which a remnant core could persist long enough to produce observable signatures. A more detailed, fully quantitative treatment of mass loss, dissolution depths, and erosion timescales lies beyond the scope of the present study and will be addressed in future dedicated work.

4.3 Non-standard solar models

The chemical evolution of the protoplanetary disk affects the young Sun in two principal ways. Heavy elements are incorporated into planetesimals and planets, while the remaining hydrogen- and helium-rich gas may continue to accrete onto the stellar surface. This process modifies the metallicity of the stellar convective envelope, with the magnitude of the change depending on its mass. If a planet later migrates inward and is engulfed by the star, metal-rich material is returned to the stellar envelope. The combined effects of metal-poor gas accretion and subsequent planet engulfment can therefore modify the sound-speed profile near the base of the solar convection zone.

Planet engulfment is an intrinsically dynamical process that is expected to produce transient energy release. Hydrodynamic simulations of planet engulfment predict transient energy deposition and surface luminosity enhancements driven by shock heating and drag dissipation during inspiral (e.g., Mustill & Villaver (2012); MacLeod & Ramirez-Ruiz (2015); Staff et al. (2016)). These transient responses are not localized thermonuclear burning events but rather rapid structural adjustments that can manifest as short-lived brightening episodes.

In this work, we restrict our analysis to early-stage planetary engulfment involving low-mass planets, occurring when the proto-Sun possessed a deep and massive convective envelope. By stating that such an event does not lead to extreme or disruptive long-term modifications of the global solar structure and evolution, we do not imply the absence of significant localized or compositional effects. On the contrary, planet engulfment can induce appreciable changes in the chemical composition of the convective envelope, and consequently in opacity and surface abundances. However, for low-mass planets engulfed during the fully convective or early pre-main-sequence phase, previous studies indicate that these effects are efficiently diluted and do not produce persistent, large-scale alterations to the stellar evolutionary track or interior sound-speed profile (e.g. Siess & Livio (1999); Baraffe et al. (2010); Théado & Vauclair (2012)). This assumption is not intended to apply to more massive or metal-rich planets, or to engulfment events occurring after the retreat of the convective zone, where structural, rotational, or thermal perturbations may be longer-lived. Given the intrinsic limitations of one-dimensional stellar evolution codes in modeling the fully dynamical aspects of engulfment, we therefore focus exclusively on the chemical consequences of the event, while neglecting transient hydrodynamical and angular momentum effects.

Using the MESA code, we construct non-standard solar models by losing and accreting mass with different chemical compositions. The mass change occurs early in the solar evolution. The mass with a low abundance of heavy elements can be regarded as dust-free hydrogen and helium gas formed in the disk. The metal-rich accretion episode is introduced to represent the engulfment of planetary material and to investigate its effect on the internal chemical stratification.

The mass of the solar convective zone in the zero-age main-sequence phase is larger than that of the current Sun. As the thickness of the convective zone reduces over time, significant effort is required to ensure that the mass accreted from the surface at an early time provides the desired chemical composition gradient in the current solar model. The excess heavy elements in the radiative layer just below the convective zone increase the opacity and may render that layer convective, and the desired chemical differentiation for the solar model is eliminated. Therefore, the amount and chemical composition of the accreted mass must be carefully determined.

By introducing accretion episodes with different chemical compositions, the sound-speed difference between the Sun and the solar models can be reduced substantially (Figure 4). Among the solar models with low metallicity (Z = 0.0134), Model N is the best solar model with a very small SSD. Its surface chemical composition agrees well with the observed values (Basu & Antia 1995; Asplund et al. 2009) (see Table 2). Model D is very similar to Model N, except for its surface helium abundance. In the upper part of Figure 4, the metallicities of Models N and D are also plotted. The root-mean-square values of $\delta c/c$ for the standard model and Models N and D are 0.0040, 0.0022, and 0.0016, respectively. See Table 2 and Figure 8 to consider the differences between the solar models with high and low metallicities.

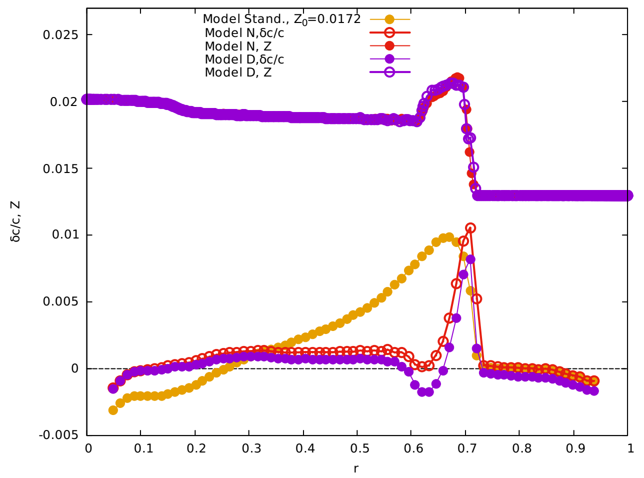

Figure 4. The difference in the speed of sound for the non-standard models. The difference in the speed of sound between the Sun and the non-standard solar models constructed using the MESA code. The standard model with $Z = 0.0172$ is also plotted (filled orange circle) for comparison. Model N and D are represented by red and purple circles, respectively. In the upper part of the figure, the metallicities of Model N and D are plotted.

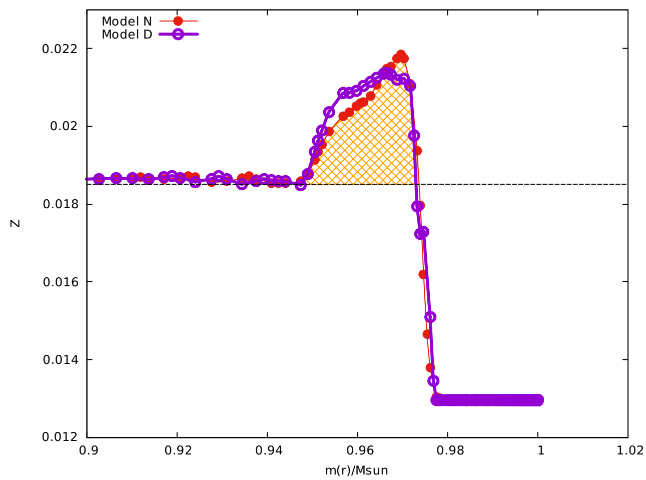

Figure 5. Metallicity versus mass for the solar models. Metallicities of Models N and D are plotted with respect to mass for the envelope. The hatched area marks the metal excess part of Model N.

4.4 Can we determine the characteristics of the engulfed planet?

The properties of the engulfed planet, particularly the mass of the heavy-element material deposited below the convection zone, can be estimated from the constructed solar models. For this purpose, computing the metallicity excess below the convective zone of Models N and D will be sufficient. The metallicity excess of the two models roughly occurs between $r = 0.6$ and 0.7 $R_{\odot}$.

In Figure 5, the metallicity of Models N and D is plotted with respect to their relative mass. The metal-enhanced region extends ($Z > 0.0185$) over the mass interval $m = 0.947 - 0.974$ $M_{\odot}$. We can calculate the total amount of metallicity excess for the two solar models. For Model N,

$$M_z = \int_{0.947M_{\odot}}^{0.974M_{\odot}} (Z - 0.0185)\,dm. \quad (2)$$

The hatched area represents the metallicity excess of Model N under the solar convection zone. We numerically evaluate this integral and compute the metallicity excess as 4.94×10^{-5} $M_{\odot} = 16.457$ $M_{\oplus}$. This heavy-element mass is comparable to the heavy-element content inferred for Neptune and therefore represents a plausible minimum estimate for the dissolved planetary material. In addition, some amount of mass settled into the lower layers ($M_{\rm set}$) and some mixed into the convective envelope ($M_{\rm mix}$). The total mass of the planet $M_{\rm p}$ can thus be expressed as

$$M_{\rm p} = M_{\rm c} + M_{\rm set} + M_{\rm mix}. \quad (3)$$

Assuming that the inferred heavy-element mass corresponds to the planetary core mass, and using the empirical relation between $M_{\rm c}$ and $M_{\rm p}$ obtained (Yıldız et al. 2024) for the gas giants in the Solar System, the total mass of the engulfed planet can be estimated as

$$\frac{M_{\rm p}}{M_{\oplus}} = 3.721 + 9.584 \times 10^{-3} \left(\frac{M_{\rm c}}{M_{\oplus}}\right)^{2.804}, \quad (4)$$

$M_{\rm p}$= 28.39 $M_{\oplus}$ = 1.6554 $M_{\rm N}$. (See Ronco et al. (2020) for the fate of inner Neptunes).

The mass of the dissolved planet in the layer below the convective zone can be estimated using a simple method. The mass of the layer is about 0.974 - 0.947 = 0.027 $M_{\odot}$. As an order-of-magnitude estimate, the metallicity excess is about 10 percent of $Z = 0.0185$. Then, the metallicity excess in one gram of matter is about 0.00185. By multiplying 0.00185 with 0.027 $M_{\odot}$, we can approximate the mass of the dissolved planet as 5×10^{-5} $M_{\odot}$. This value is very close to that derived from the numerical integration of equation (2) for Model N.

The metallicity excess below the convective zone of Model D is also numerically integrated as $M_{\rm c}$ = 17.56 $M_{\oplus}$ = 1.024 $M_{\rm N}$. The total mass of the planet is estimated as $M_{\rm p}$ = 33.31 $M_{\oplus}$ = 1.942 $M_{\rm N}$. Then, the difference between the $M_{\rm c}$ of Models N and D can be regarded as the typical uncertainty of $M_{\rm c}$; $M_{\rm c} = 0.960 \pm 0.064$ $M_{\rm N}$. Similarly, $M_{\rm p} = 1.65 \pm 0.29$ $M_{\rm N}$.

4.5 Physical interpretation of planetary disruption during engulfment

Once a planet is engulfed by the Sun, its subsequent evolution is governed by hydrodynamic drag, thermal ablation, and ram-pressure stripping within the stellar envelope. In this regime, the interaction differs fundamentally from that of a detached two-body system in orbit, and the engulfed planet should not be treated as a stable binary component. Instead, orbital energy is rapidly dissipated, causing the planet to sink toward deeper layers while progressively losing mass.

Because the mean density of the engulfed planet generally exceeds that of the outer stellar envelope, it can initially penetrate inward before significant disruption occurs. As the ambient stellar density and temperature increase, hydrodynamic stripping and thermal erosion become increasingly efficient, ultimately leading to fragmentation and dissolution of the planet. The depth at which this process becomes dominant depends sensitively on the internal density, composition, and structural integrity of the planet, as well as on the local properties of the stellar envelope.

In this work, we do not attempt to model the detailed mass-loss history or the dynamical evolution of the engulfed planet, as such processes are inherently multidimensional and time-dependent. Instead, we use the location of the maximum sound-speed perturbation, δc, as an empirical indicator of the region where the deposited planetary material most strongly affects the solar interior. This approach allows us to link the inferred chemical signatures to a plausible engulfment depth without invoking a specific dynamical disruption mechanism.

Hydrodynamic simulations indicate that dense planetary cores may penetrate below the convective envelope before undergoing substantial erosion, whereas lower-density planets are expected to fragment and mix efficiently within the convective region or near its base. The present analysis is therefore intended to capture the chemical consequences of engulfment rather than to provide a detailed physical model of planetary disruption, which lies beyond the scope of one-dimensional stellar evolution calculations.

4.6 Non-standard solar model with the recent solar high metallicity

Despite decades of intensive study, the solar chemical composition remains one of the most controversial properties of the Sun. Estimates of the solar heavy-element abundance have changed considerably over the past two decades. A recent study (Magg et al. 2022) found the Z/X ratio to be 0.0225 ± 0.0014, bringing the inferred solar metallicity back to values comparable to those obtained about a quarter of a century ago. If $Y_s = 0.2485$, $Z_s = 0.0165 \pm 0.0010$.

New non-standard solar models under this metallicity constraint are constructed by losing and accreting mass twice. In our models, two distinct mass-accretion episodes are considered, motivated by physical rather than fine-tuning arguments. Accretion associated with planet engulfment is expected to be metal-rich and would further increase the surface metallicity of an already metal-rich standard solar model, leading to a significant mismatch with the observed solar surface abundances. A subsequent low-metallicity accretion episode is therefore required to reconcile the surface composition with observational constraints. Such metal-poor accretion is physically plausible, as planet formation sequesters heavy elements into solid bodies, leaving behind a residual gas reservoir that is depleted in metals and can later be accreted by the host star. This sequence of accretion events allows the models to satisfy both helioseismic constraints and surface abundance measurements. See Section 4.15 for the solar models without mass-loss and with two mass accretions and M_i=0.97 $M_\odot$.

M_i of Models Zz190, Yz197, NCz190, NCz187, and NCz195 is 1.05 $M_\odot$. While the first two models are constructed using the linear interpolation method for opacity computation, the cubic method (`cubic_interpolation_in_Z` and `cubic_interpolation_in_X` options in MESA) is used for the remaining models. The model with $Z_0 = 0.0190$, which contains a localized high-metallicity region below the convection zone, has $Z_s = 0.0168$ and $Y_s = 0.2493$ (Model Zz190 in Table 2). Although the agreement between the model and the observed solar sound-speed profile is greatly improved relative to Model N (Figure 6), the resulting convection-zone base ($R_{bcz} = 0.7199$ $R_\odot$) remains appreciably larger than the helioseismic value of 0.713 $R_\odot$. The mass of the engulfed planet is computed as 0.73 M_N.

Since the sound speed is inversely proportional to the square root of the mean molecular weight, an alternative way of reducing the sound-speed discrepancy is to decrease the helium abundance below the convection zone instead of introducing a metallicity enhancement. Such a model is given in Table 2 (Model Yz197). SSD between this model and the Sun is also plotted in Figure 6a. It is in very good agreement with the observational solar sound speed. Its R_{bcz} (0.7203 $R_\odot$) is significantly greater than the observed value 0.713 $R_\odot$ despite its relatively high initial metallicity. Y profiles of the standard model, Models N, Zz190, and Yz197 are plotted in Figure 6b.

Mass exchange between the proto-star and its surrounding disk has two principal consequences: (i) if the accreted material has a different chemical composition, the stratification immediately below the convection zone is modified; (ii) the amount of accreted and lost material changes the location of the convection-zone base. These effects change the chemical composition of the star's outer layers. These changes directly affect both the sound-speed profile and the depth of the convection zone. R_{bcz} of the non-standard models with high metallicity is in better agreement with the observed value, but still, there is a significant difference between them if the linear interpolation method is applied.

SSD strongly depends on the initial metallicity of the models. The models with $Z_0 \approx 0.0190$ give results compatible with the solar data. However, there is a very sharp metallicity gradient just below the solar convection zone. For the previous models, the linear interpolation technique is applied for opacity calculations from the tables. New solar models with cubic interpolation and with different metallicities are constructed to explain which value of Z gives the best solar model. The SSDs of the models with $Z_0 = 0.0187$ (Model NCz187), 0.0190 (Model NCz190), and 0.0195 (Model NCz195) are plotted against r in Figure 7. The higher the metallicity, the better the agreement between the model and the Sun. The best agreement is obtained with $Z = 0.0195$ (Model NCz195). The R_{bcz}, Y_s, and Z_s of this model are also listed in Table 2 and are in excellent agreement with the helioseismic and spectroscopic data. Among the models investigated in this work, Model NCz195 provides the best simultaneous agreement with the helioseismic and spectroscopic constraints.

The metallicity enhancement in the best-fitting model extends from approximately $r = 0.67$ to $r = 0.7$ $R_\odot$ (m =0.96-0.973 $M_\odot$). From the integration of this metallicity excess, we compute the mass of the dissolved planet as 1.00 M_N. From equation (4), we can estimate the total mass of the engulfed planet as 1.83 M_N.

4.7 Non-standard solar models with $M_i = 1$ $M_\odot$

M_i of Models NCz197 and NCz198 in Table 2 is 1.0 $M_\odot$. R_{bcz} of these models are in very good agreement with the observed value thanks to the high Z_0 and the cubic interpolation method. Z_0 of Models NCz197 and NCz198 is 0.0197 and 0.0198, respectively. $\delta c/c$ for these models is plotted in Figure 8a. These two models, together with Model NCz195 with $M_i = 1.05$ $M_\odot$ are in very good agreement with the Sun. Comparing the R_{bcz}, Y_s, and Z_s of Model NCz198 with those of the Sun, we find that Model NCz198 is very similar to the best solar model (Model NCz195). However, the computed mass of the engulfed planet for Model NCz198 is significantly lower than that of Model NCz195. This comparison suggests that the inferred planetary mass depends sensitively on the assumed metallicity of the deep solar interior. The dissolved planet mass of Model NCz198 is broadly consistent with the estimates of the findings of Martin & Livio (2016).

The adiabatic sound speed is given by

$$c = \sqrt{\Gamma_1 \frac{P}{\rho}}. \quad (5)$$

Γ_1 and P/ρ of Model NCz195 and Model NCz198 are plotted in the middle and lower panels of Figure 8, respectively. For comparison, Model StZ190 is also plotted. While Γ_1 of the non-standard models is less than that of the standard solar model below the convective zone, the P/ρ ratio for the non-standard models is greater than that

Table 2. Basic properties of the solar models and mass of the engulfed planet. Z_0 and Y_0 of the non-standard solar models are listed in the second and third columns, respectively. $M_{\rm i}$ is given in the fourth column. The mixing-length parameter α, $Z_{\rm s}$, and $Y_{\rm s}$ for the non-standard solar models are given in the fifth, sixth, and seventh columns, respectively. The central compositions of the models are given in the eighth and ninth columns, respectively. The tenth and eleventh columns are for the central density and temperature, respectively. While the twelfth column is for the maximum SSD below the convective zone, the mean SSD is given in the thirteenth column. $R_{\rm bcz}$ is given in the fourteenth column. The mass of the planet in the process of being engulfed and dissolved is listed in the other columns. The bottom part of the table is for the solar models with high metallicity (Magg et al. 2022). The best model we obtained is Model NCz195, whose Z_0 is 0.0195 and whose opacity calculation is done by the cubic interpolation method. $M_{\rm c}$ of this model is found as 1.00 $M_{\rm N}$. Model NCz198 is very similar to Model NCz195. We test effects of turbulent mixing, thermohaline mixing, different EOSs, opacities, and different parametrization of α. Three models in the last three rows are the best of the best models (see Section 4.14). These models are constructed considering both mass transfer (and loss) and turbulent mixing. The inlist and model files (in GONG format) of Models NCZ198 and PTMv6 are uploaded to GitHub.

Model	Z_0	Y_0	$M_{\rm i}$ $M_\odot$	α	$Z_{\rm s}$	$Y_{\rm s}$	$X_{\rm c}$	$Z_{\rm c}$	$\rho_{\rm c}$ g/cm^3	$T_{\rm c}$ MK	$\lvert(\delta c/c)_{\rm max}\rvert$	$\overline{\delta c/c}$	$R_{\rm bcz}$ $R_\odot$	$M_{\rm c}$ $M_\oplus$	$M_{\rm c}$ $M_{\rm N}$	$M_{\rm p}$ $M_\oplus$	$M_{\rm p}$ $M_{\rm N}$
Model N	0.0190	0.2837	1.20	1.7257	0.0130	0.246	0.3421	0.0202	149.9	15.76	0.0106	0.00103	0.7334	16.5	0.96	28.4	1.66
Model D	0.0190	0.2837	1.20	1.7765	0.0129	0.234	0.3424	0.0202	149.8	15.76	0.0082	0.00028	0.7247	17.6	1.02	33.3	1.94
Obs.	—	—	—		0.0134	0.2485	—	—	—	—	—	—	0.713	—	—	—	—
Model Zz190	0.0190	0.2857	1.05	1.8652	0.0168	0.2493	0.3364	0.0202	151.7	15.85	0.063	0.00043	0.7199	12.5	0.73	15.2	0.89
Model Yz197	0.0197	0.2913	1.05	1.9161	0.0184	0.2474	0.3255	0.0209	154.2	15.98	0.0047	-0.00013	0.7203	—	—	—	—
Model NCz190	0.0190	0.2869	1.05	1.8706	0.0166	0.2493	0.3347	0.0202	152.2	15.87	0.0056	0.00031	0.7152	7.8	0.45	7.8	0.45
Model NCz187	0.0187	0.2854	1.05	1.8619	0.0163	0.2480	0.3369	0.0199	152.0	15.84	0.0059	0.00049	0.7172	6.3	0.37	6.3	0.37
Model NCz195	0.0195	0.2892	1.05	1.8929	0.0172	0.2485	0.3325	0.0209	152.1	15.89	0.0055	0.00004	0.7133	12.1	0.70	14.1	0.82
Model NCz197	0.0197	0.2904	1.00	1.8927	0.0171	0.2491	0.3308	0.0209	152.3	15.91	0.0057	-0.00009	0.7133	8.8	0.51	8.8	0.51
Model NCz198	0.0198	0.2910	1.00	1.9010	0.0168	0.2484	0.3287	0.0210	152.5	15.93	0.0057	-0.00008	0.7130	9.6	0.56	9.6	0.56
Model EOPAL	0.0197	0.2920	1.00	1.8804	0.0166	0.2496	0.3297	0.0209	153.0	15.93	0.0057	-0.00005	0.7167	8.2	0.48	8.2	0.48
Model OPgs98	0.0199	0.2770	1.05	1.9013	0.0170	0.2484	0.3457	0.0211	152.0	15.71	0.0053	0.00017	0.7184	6.3	0.37	6.3	0.37
Model OPgs98z1	0.0199	0.2769	1.05	1.8995	0.0163	0.2490	0.3460	0.0211	151.9	15.71	0.0058	0.00017	0.7183	5.4	0.31	5.4	0.31
Model OPgs98z2	0.0199	0.2772	1.05	1.8784	0.0166	0.2485	0.3451	0.0211	152.2	15.72	0.0056	0.00001	0.7190	9.6	0.56	9.6	0.56
Model MLTa	0.0195	0.2892	1.05	1.9129	0.0177	0.2499	0.3283	0.0207	153.5	15.93	0.0024	0.00007	0.7137	8.1	0.47	8.1	0.47
Model MLTc	0.0195	0.2889	1.05	1.9148	0.0179	0.2486	0.3292	0.0207	153.2	15.91	0.0018	0.00008	0.7111	6.4	0.37	6.4	0.37
Model MLTatF0	0.0195	0.2889	1.05	1.9068	0.0175	0.2488	0.3291	0.0207	153.2	15.92	0.0018	0.00001	0.7190	8.8	0.51	8.8	0.51
Model MLTatF3	0.0195	0.2894	1.05	1.8944	0.0172	0.2490	0.3309	0.0207	152.6	15.91	0.0032	0.00016	0.7155	8.0	0.46	8.0	0.46
Model MLTatF4	0.0195	0.2894	1.05	1.8944	0.0171	0.2482	0.3319	0.0207	152.3	15.90	0.0043	0.00015	0.7153	7.9	0.46	7.9	0.46
Model MLTaA	0.0198	0.2903	1.05	1.9143	0.0176	0.2492	0.3272	0.0210	153.3	15.94	0.0017	0.00029	0.7141	10.1	0.59	10.1	0.59
Model MLTaB	0.0198	0.2903	1.05	1.8980	0.0171	0.2488	0.3271	0.0210	153.3	15.94	0.0029	0.00001	0.7137	8.4	0.49	8.4	0.49
Model PTM63	0.0198	0.2903	1.05	1.9095	0.0175	0.2501	0.3272	0.0210	153.3	15.94	0.0026	0.00032	0.7143	8.5	0.49	8.5	0.49
Model PTM67	0.0198	0.2903	1.05	1.9095	0.0173	0.2479	0.3272	0.0210	153.3	15.94	0.0020	0.00029	0.7142	9.9	0.58	9.9	0.58
Model PTM71	0.0198	0.2903	1.05	1.9095	0.0172	0.2462	0.3272	0.0210	153.3	15.94	0.0021	0.00002	0.7142	10.0	0.58	10.0	0.58
Model PTMv8	0.0198	0.2903	1.05	1.9095	0.0174	0.2484	0.3272	0.0210	153.3	15.94	0.0011	0.00017	0.7142	8.6	0.50	8.6	0.50
Model PTMv7	0.0197	0.2898	1.05	1.8939	0.0169	0.2492	0.3278	0.0209	153.3	15.93	0.0010	0.00012	0.7141	10.5	0.61	10.5	0.61
Model PTMv6	0.0196	0.2894	1.05	1.9126	0.0176	0.2477	0.3283	0.0208	153.3	15.93	0.0008	0.00012	0.7116	7.2	0.42	7.2	0.42
Model DD1020	0.0195	0.2892	0.97	1.8995	0.0170	0.2482	0.3283	0.0208	153.3	15.92	0.0008	0.00037	0.7134	5.6	0.33	5.6	0.33
Model DD1020p	0.019475	0.2888	0.97	1.8897	0.0169	0.2484	0.3296	0.0207	153.1	15.91	0.0007	0.00014	0.7140	4.6	0.27	4.6	0.27
Model DD0525	0.0195	0.2888	0.97	1.8923	0.0170	0.2485	0.3298	0.0207	153.0	15.91	0.0009	-0.00007	0.7139	4.9	0.29	4.9	0.29
Model DD0525p	0.0195	0.2891	0.97	1.8950	0.0170	0.2495	0.3292	0.0207	153.2	15.92	0.0007	-0.00003	0.7161	5.8	0.34	5.8	0.34
Model PureENGF	0.0192	0.2877	0.97	1.8924	0.0168	0.2480	0.3312	0.0204	153.0	15.89	0.0025	0.00002	0.7132	7.8	0.45	7.8	0.45
Model TurMixaV	0.0190	0.2864	1.00	1.8470	0.0180	0.2670	0.3332	0.0202	152.7	15.87	0.0022	0.00036	0.7199	—	—	—	—
Obs.	—	—	—	—	0.0165	0.2485	—	—	—	—	—	—	0.713	—	—	—	—
Unc. Obs.	—	—	—	—	0.0010	0.0034	—	—	—	—	—	—	0.001	—	—	—	—

of the standard model in the same region. Because the increase in P/ρ exceeds the decrease in Γ_1, the resulting sound speed agrees much better with the helioseismic measurements.

4.8 Further comparison of the solar models and the planetary masses

Table 2 summarizes the principal properties of all solar models considered in this work. The initial helium abundance increases approximately linearly with the adopted initial metallicity. More generally, Y_0 may be regarded as a function of both $M_{\rm i}$ and Z_0. There is a linear relationship between Y_0 and the central helium abundance ($Y_{\rm c} = 1 - X_{\rm c} - Z_{\rm c}$). $\rho_{\rm c}$ is most dependent on $M_{\rm i}$, while $T_{\rm c}$ is most dependent on $M_{\rm i}$ and Y_0. Since the center of the model with the most contraction will be the hottest, $T_{\rm c}$ increases as $\rho_{\rm c}$ increases.

$M_{\rm c}$, the dissolved part of the engulfed planet below the convective zone, depends on how the metallicity excess is distributed below the zone. For example, we can compare the metallicity excesses of Model N and Model Zz190. The Z excess of Model N increases almost linearly between r = 0.6 and 0.7 $R_\odot$, while the metallicity excess of Model Zz190 ranges from approximately r = 0.65 $R_\odot$ to 0.7 $R_\odot$. The former model has an $M_{\rm c}$ of 0.96 $M_{\rm N}$, while the latter has a $M_{\rm c}$ of 0.73 $M_{\rm N}$. Thus, the deeper the metallicity enhancement extends below the convection zone, the larger the inferred dissolved planetary mass.

However, Model N and Model Zz190 have the same Z_0. If Z_0 of two models is not the same, then the metallicity excess depends on Z_0. For models with different initial metallicities, however, the inferred dissolved planetary mass also depends on the adopted Z_0, decreasing as Z_0 increases.

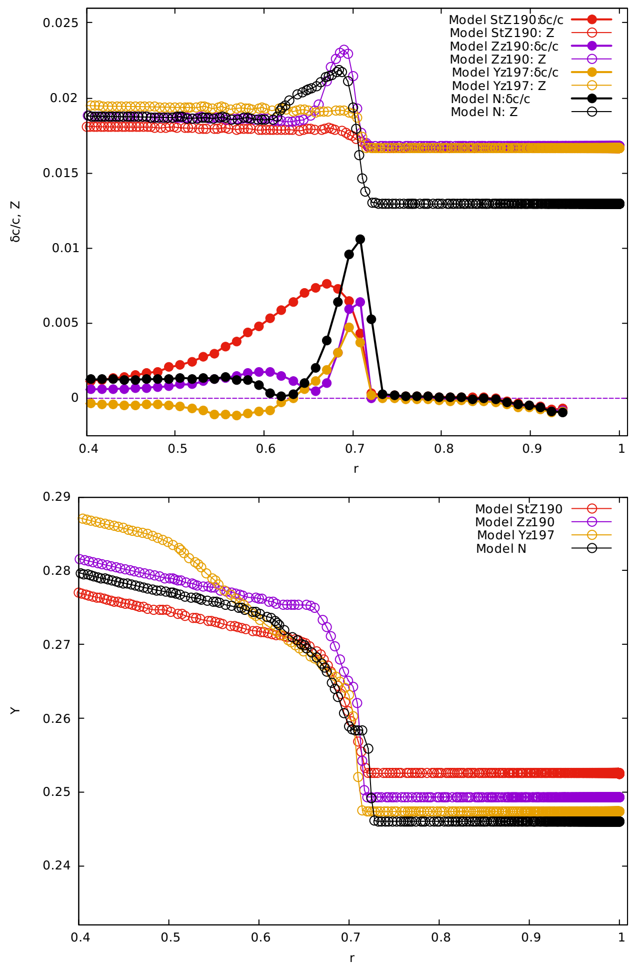

Figure 6. (*a*) The difference in the speed of sound, Z, and Y for the non-standard models with different Z and Y profiles. The standard model with $Z = 0.0190$ is also plotted (filled orange circle) for comparison. Model N and D are represented by red and blue circles, respectively. In the upper part of the figure, the metallicities of Model N and D are plotted. (*b*) The helium profiles of these models are plotted.

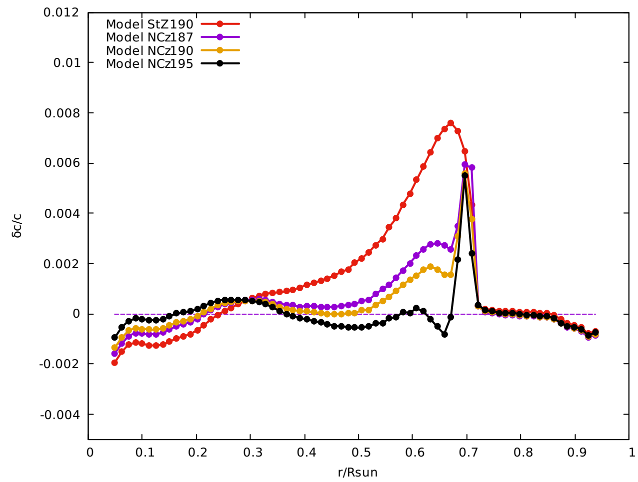

Figure 7. Sound speed difference between the Sun and the solar models. The sound speed difference between the Sun and the solar models with different initial metallicities is plotted with respect to the radius. These models are in agreement with the metallicity found by Magg et al. (2022). The best agreement is obtained with $Z_0 = 0.0195$. The initial mass of the non-standard models is 1.05 $M_\odot$. The cubic interpolation is used for the non-standard models.

4.9 Effect of different opacities on the standard and non-standard solar models

Planetary engulfment provides an unconventional but promising mechanism for improving solar models. To assess the robustness of this mechanism, we test different opacity tables and equations of state available in MESA to determine whether the planetary-engulfment (or Z-bump) scenario consistently improves the models. The role of the MLT parameter in these tests must also be established (see Section 4.11).

For the stellar interior, the alternative opacity to the OPAL opacity is the OP opacity (Seaton 2005). The standard (Table 1) and non-standard solar models (Tables 2 and 3) are constructed using two different mixtures, namely A09 and GS98. For the standard solar models with GS98, different constraints require different metallicities: for Z_s and Y_s, Z_0 should be 0.0180 and 0.0199, respectively; for R_{bcz}, $Z_0 > 0.025$.

Three representative non-standard models computed with the OP opacity tables and Z_0=0.0199 are listed in Table 2 (Models OPgs98, OPgs98z1 and OPgs98z2). The mass accretion and loss processes of Model OPgs98 are very similar to that of Model NCz195, except for the times of mass losses and the second accretion. The second mass accretion of Model NCz195 and OPgs98 starts at 51.5 and 61.5 Myr, respectively.

The difference between Models OPgs98 and OPgs98z1 is mainly due to different metallicity of the accreted masses (Z_{acc}). The metallicity of the first (Z_{acc1}) and second (Z_{acc2}) accreted mass of Model OPgs98 (OPgs98z1) is Z_{acc1}=0.070 (0.030) and Z_{acc2}=0.008 (0.013), respectively. For Model OPgs98z2, Z_{acc1} =0.0414 and Z_{acc2} =0.0121. The results of different metallicities are seen in Figure 9 and Table 2. The Z_s and Y_s of these three models range 0.0163-0.0170 and 0.2484-0.2490, respectively, and are in good agreement with the observed values. However, the convective zones of these models are shallower than the value found from the helioseismic analysis, about 0.005-0.006 $R_\odot$.

Z and $\delta c/c$ of these three models are plotted in Figure 9. For comparison, the non-standard Model NCz195 and the standard model with Z_0=0.0188 (similar to the BP04 model of Bahcall & Pinsonneault (2004)) are also plotted in Figure 9. These three models differ primarily in the metallicity of the accreted material and, consequently, in the shape and extent of the metallicity enhancement below the convection zone. For each Z_{acc1}, there is an optimal accretion time to minimize $\delta c/c$. Those with low Z_{acc1} penetrate deeper, while those with high Z_{acc1} confine excess metal to a narrow region below the convective zone. These models favor an engulfed planet with a mass in the super-Earth regime (~ 5-10 $M_\oplus$). Model OPgs98, a model closer to Model N, has a planetary mass of 6.3 $M_\oplus$ (see Table 2).

The most significant difference between models built with OPAL and OP opacity is the R_{bcz} of the models. Although the R_{bcz} of models using the OPAL table is more consistent with observation, the R_{bcz} of models with OP is 0.005-0.006 $R_\odot$ higher than the observed value. Although the OP opacity tables predict a slightly shallower convection zone than observed, the planetary-engulfment (or Z-bump) scenario still produces a substantial improvement over the corresponding standard solar models.

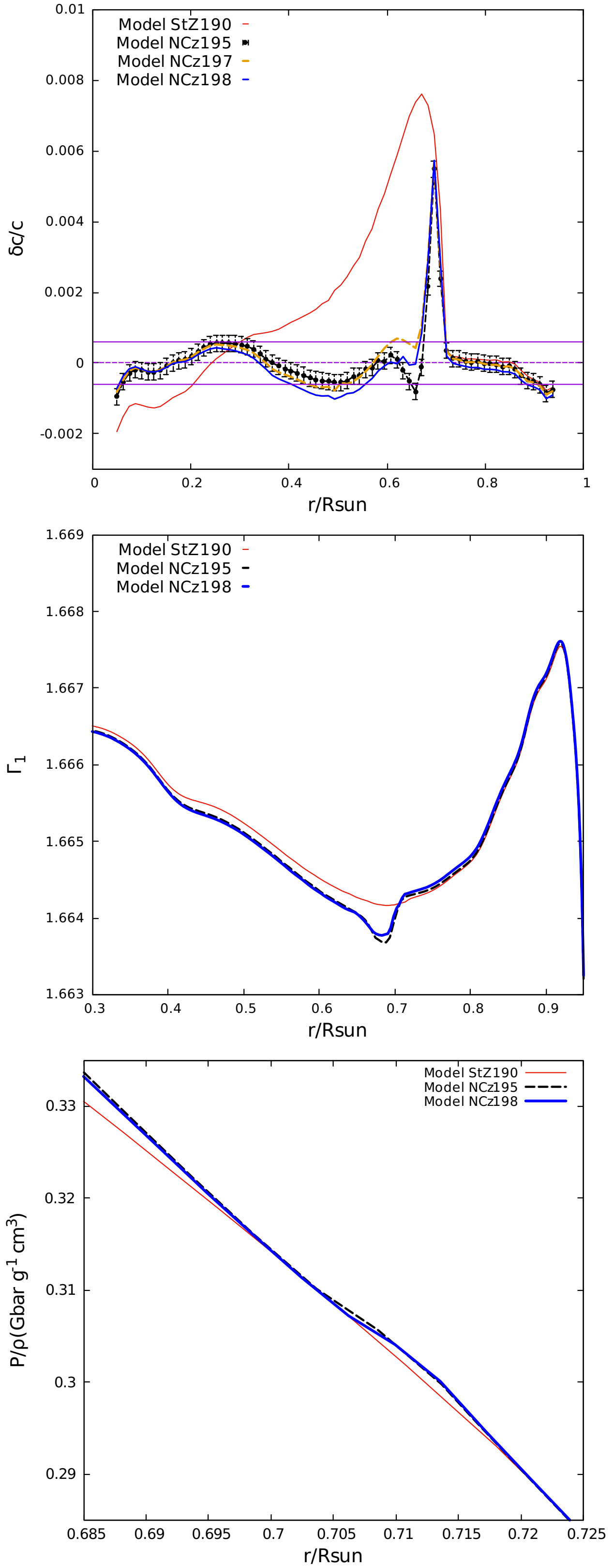

Figure 8. (*a*) The sound speed difference is plotted with respect to r for the solar models with different initial masses. The thick and solid lines are for the models with $M_{\rm i}$ = 1.00 and $M_{\rm i}$ = 1.05 M$_\odot$, respectively. The best agreement between the models and the Sun is obtained with Z_0 = 0.0198 and Z_0 = 0.0195. For Model NCz195, the difference is less than 0.0006, except for the very narrow region just under CZ. For comparison, Model StZ190 is also plotted. (*b*) Γ_1 and (*c*) P/ρ of the solar models are also plotted respect to r around the base of the solar convective zone.

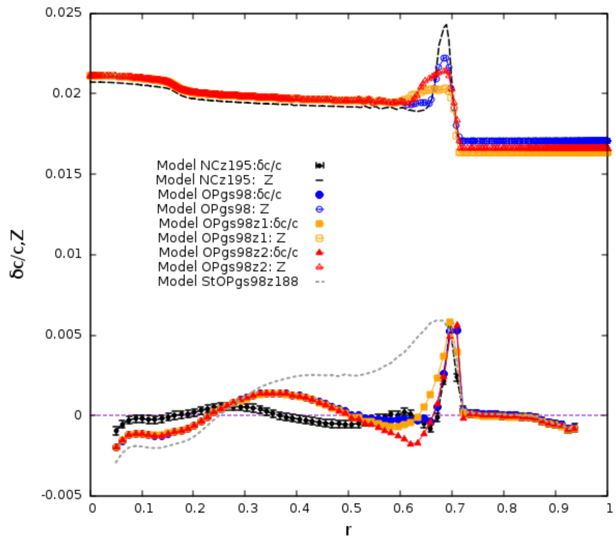

Figure 9. The sound speed difference and metallicity are plotted with respect to r for the non-standard solar models with the OP opacity tables with Z_0 = 0.0199. For the GS98 mixture, the maximum sound speed difference between the Sun and the solar models are about 0.006. The main differences between these models are the time of first accretion and metallicity of the accreted material. For the most suitable Model OPgs98, accretion stars at 21.2 Myr and Z = 0.07. The accretion time for Models OPgs98z1 and OPgs98z2 is 20.2 (Z = 0.03) and 20.5 Myr (Z = 0.0414), respectively. For comparison, the standard solar model with Z=0.0188 and Model NCz195 are also plotted.

4.10 Effect of different EOSs

The default EOS for the solar models in MESA is based on the FreeEOS code developed by Irwin (2012). To test the effect of EOS on the solar models and the results for the engulfed planet, we also construct standard and non-standard solar models with the OPAL EOS. The initial metallicity and mass of the non-standard model is Z_0=0.0197 and $M_{\rm i}$=1.00 M$_\odot$ (Table 2), respectively. ($\delta c/c$) and Z of the best non-standard model we obtain are plotted in Figure 10. For comparison, also shown are Model NCz195 and the standard model with OPAL EOS and Z_0=0.0188. It is evident that the planet-engulfment scenario substantially improves the agreement between the solar model and the helioseismic sound-speed profile, particularly over the radial range r =0.5-0.7 R$_\odot$. The principal limitation of this model is that the base of the convection zone remains at $R_{\rm bcz}$ ≈ 0.7167 R$_\odot$, about 0.0037 R$_\odot$ shallower than the helioseismically inferred value. For this model, the engulfed planet is a super-Earth, with a mass of 8.2 M$_\oplus$.

4.11 Effects of different α parametrizations

The mixing-length parameter α is usually calibrated by reproducing the present-day solar radius and luminosity. The solar α value generally depends on the chosen metallicity. For example, for standard solar models, Z_0 =0.016 and 0.020, it is around α=1.82 and 1.89 (Yıldız 2008), respectively. Whether α is universal or varies with stellar mass and evolutionary state remains an active topic of investigation (Tayler 1986; Ludwig, Freytag, & Steffen 1999; Yıldız et al. 2006; Joyce & Tayar 2023; Ocampo et al. 2025). As the value of α increases, convective efficiency increases, facilitating energy escape from the star and decreasing the model radius. The value of α in the early stages of mass transfer is also important because mass of the

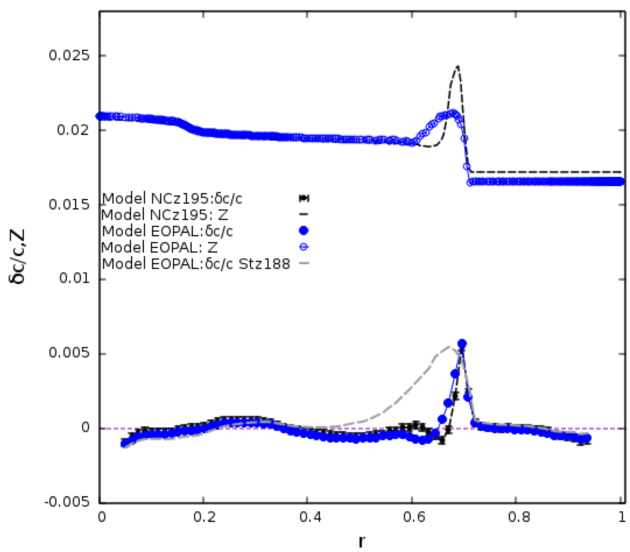

Figure 10. The sound speed difference (filled circle) and Z (circle) are plotted with respect to r for the non-standard solar model with the OPAL EOS. For comparison, Model NCz195 with error bars and the standard model with OPAL EOS and Z_0=0.0188 (dashed line) are also plotted.

convective zone in the early phase of the solar evolution depends also on α.

Several observational and theoretical studies suggest that α is unlikely to remain constant for all stars or throughout stellar evolution. Yıldız et al. (2006), in their detailed study of Hyades binary stars, found that α is highly dependent on M (or effective temperature) for MS stars. A study on the α Centauri system (Figures 5 and 6 in Yıldız (2007)) indicates that α can increase or decrease over time.

α is taken as a constant during the evolution of solar models with high initial mass ($M_{\rm i}$ = 1.2 $M_\odot$). To obtain a steep metallicity gradient below the CZ, we use a small value of α (1.365) for models with low $M_{\rm i}$ (1.00-1.05 $M_\odot$) in the early phase of evolution for Models NCz190-OPgs98z2 in Table 2. At a later time (4.4 Gyr), α increases to a higher value to calibrate the model radius, given in Table 2. This is the case for Models MLTa and MLTc. $\delta c/c$ and Z of these two models are plotted in Figure 11a. They are very similar models; the slight differences between them are due to slight differences between their mass accretions and losses. The most important difference appears between their $R_{\rm bcz}$, although their Z profiles below the CZ are very similar. This implies that $R_{\rm bcz}$ is a very sensitive function of the Z profile below the CZ.

We employ the standard implementation of MESA. Consequently, each change in α requires restarting the evolutionary calculation with the updated parameter. Although a continuously varying α would be more realistic, implementing such a prescription is beyond the capabilities of the current calculation setup. To simplify the situation, we obtain 4 more models with different time dependence of α, Models MLTatF0, MLTatF2, MLTatF3, and MLTatF4 (see Table 2). For all of the models α = 1.365 in the early phase of solar evolution. For Model MLTatF0, α is the calibrated value given in Table 2 for t > 0.14 Gyr. For Models MLTatF2, MLTatF3, and MLTatF4, α is changed at 2.4, 3.4, and 4.4 Gyr. Models MLTatF0, MLTatF3, and MLTatF4 are plotted in Figure 11b. Model MLTatF0 is the best among these models in terms of compatibility with the speed of sound and the sun, while Models MLTatF3 and MLTatF4 are more compatible with the

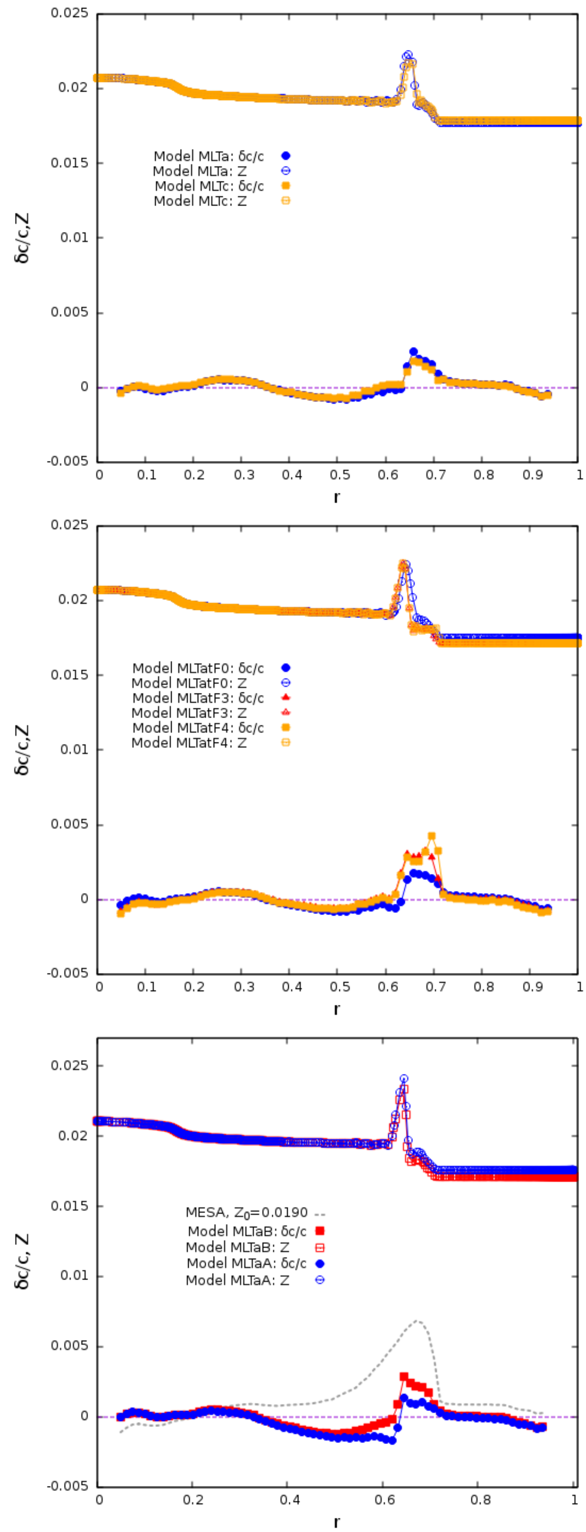

Figure 11. The sound speed difference (filled circle) and Z (circle) are plotted with respect to r for the non-standard solar models with variable α. a) α =1.365 for t < 4.4 Gyr and α is equal to the calibrated value given in Table 2. The mass transfer processes are different for Models MLTa (circle) and MLTc (circle in gray; orange in the online version). b) The transition time from low-α to high-α is 0.14, 3.4, and 4.4 Gyr for Models MLTatF0 (circle), MLTatF3 (trianle), and MLTatF0 (square). c) The initial value of $alpha$ = 1.8929. Zs of the first accretion of Models MLTaB (square) and MLTaA (circle) are slightly different.

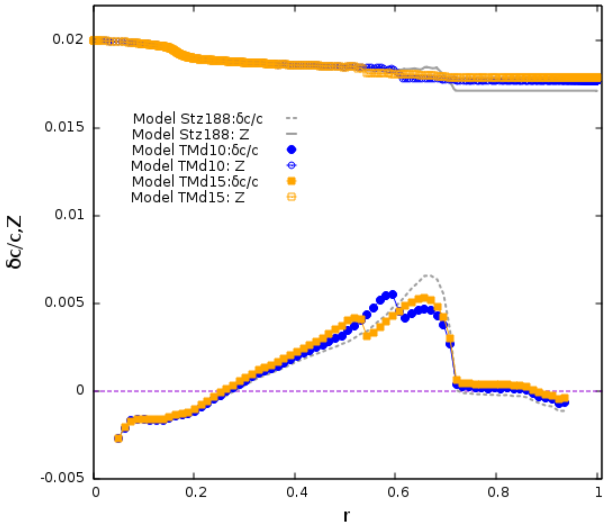

Figure 12. The sound speed difference and metallicity are plotted with respect to r for the solar models with turbulent mixing. The circles represent the model with effective depth below the convective zone is about 0.1 $R_\odot$, and the squares are for the depth of about 0.15 $R_\odot$. These models are constructed with OPAL opacity with the GS98 mixture. For comparison, the standard solar model with Z=0.0188 is also plotted, which is very similar to the BP04 model. The inclusion of turbulent mixing provides partial improvement of solar models, depending on the effective depth. However, there is some increase in $\delta c/c$ below the respective depth in both models.

Sun when considering $R_{\rm bcz}$. All of these models give the engulfed planet as a super-Earth, $M_{\rm p} \approx 8$ $M_\oplus$.

The calibrated value of α is about 1.9. We take α as the calibrated value of Model NCz195 (1.8929) in the early phase of solar evolution and construct two more models, namely Models MLTaA and MLTaB. $\delta c/c$ and Z of these two models are plotted in Figure 11c. The differences between them are due to the different metallicities of the first accretions with high metallicity. Z is 0.15 and 0.14 for Models MLTaA and MLTaB, respectively. $\delta c/c$ of these models depend on Z in the range of r =0.6-0.7 $R_\odot$. The global structural properties of these models remain remarkably similar. Mass of the engulfed planet of Model MLTaA is 1.7 $M_\oplus$ higher than that of Model MLTaB.

4.12 Effect of turbulent mixing

Turbulent mixing below the solar convection zone remains one of the major uncertainties in solar interior modelling (Brun et al. 2002; Buldgen et al. 2025). Richer, Michaud, & Turcotte (2000) performed detailed evolutionary model calculations by varying the turbulence in the outer regions of the star to improve agreement with the anomalies observed in AmFm stars. They modified the density dependence of the turbulent mixing external mass and the turbulent dissipation coefficient. They showed that the anomalies depend on a single parameter characterizing turbulence: the depth of the turbulently mixing region.

Standard solar models may be missing possible mixing processes due to turbulent motions in the Sun. The observed depletion of lithium, while preserving most of the beryllium abundance, has long been interpreted as indirect evidence for additional mixing beneath the convection zone. Brun et al. (2002) states that the sound speed difference decreases significantly due to mixing at the tachocline. The exact physical origin of turbulent mixing is yet unknown (Kunitomo, Buldgen, & Guillot 2025). The macroscopic mixing at the base of the convection zone reduces the microscopic diffusion by 25 percent compared to a purely microscopic model. There are numerous studies in the literature testing the enhanced diffusion (Guzik, Watson, & Cox 2005; Montalbán et al. 2004). While the physical justifications for these increases are debatable, the conclusions from these studies are generally that some parameters are compatible while others are not.

We construct two different models that account for turbulent mixing at different depths. In the MESA code, the minimum depth for turbulent mixing ($m_{\rm tm}$) is chosen based on mass (`mass_lower_limit_for_min_D_mix`). Figure 12 plots $\delta c/c$ versus r for these models. For Model TMd10, turbulent mixing is effective at a depth of about 0.1 $R_\odot$ at the base of the convective zone, while for Model TMd15, this depth is ~0.15 $R_\odot$. The basic properties of these models are listed in Table 3. Although there is a limited improvement in model c at these depths, the reverse occurs slightly below this depth. Turbulent mixing alone is therefore insufficient to reconcile solar models with all observational constraints, but it may provide an important secondary correction when combined with the planet-engulfment scenario (see Section 4.14).

Table 3. Basic properties of the solar models with turbulent and thermohaline mixing. These models are constructed with the OPAL opacity with the GS98 mixture. Models TMd10 and TMd15 are the models in which turbulent mixing is effective at depths of about 0.10 and 0.15 $R_\odot$ below the convective zone, respectively. The solar models with thermohaline mixing are given in the third and fourth rows (see the text). The observed values for the Sun's surface composition are given in the last row.

Model	α	Z_0	Y_0	$Z_{\rm s}$	$Y_{\rm s}$	$R_{\rm bcz}$	$(\delta c/c)_{\rm max}$
TMd10	1.85421	0.0188	0.27160	0.0177	0.2521	0.7215	0.00548
TMd15	1.85007	0.0188	0.27166	0.0179	0.2544	0.7217	0.00530
TLKip	1.86308	0.0188	0.27165	0.0171	0.2439	0.7247	0.00701
TLBGS	1.86308	0.0188	0.27165	0.0171	0.2439	0.7247	0.00700
Stz188	1.86788	0.0188	0.27165	0.0171	0.2442	0.7228	0.00657
Obs.	——	——	——	0.0165	0.2485	0.713	——
Unc.	——	——	——	0.0010	0.0034	0.001	——

4.13 Effect of thermohaline mixing

Thermohaline mixing is thought to be one of the main processes that affects surface chemical element abundances, particularly in low-mass red giant stars (Charbonnel & Zahn 2007; Denissenkov & Merryfield 2011; Nguyen et al. 2025). Ulrich (1972) treated thermohaline mixing as a diffusive process based on the turbulent diffusivity produced by the thermohaline instability in stellar radiation zones.

We construct two solar models with thermohaline mixing using two available options in MESA: `thermohaline_option = 'Kippenhahn'` (Kippenhahn, Ruschenplatt, & Thomas 1980) and `'Brown_Garaud_Stellmach_13'` (Brown, Garaud, & Stellmach 2013). The former model is Model TLKip, and the latter is Model TLBGS. $\delta c/c$ for these models is plotted with respect to r in Figure 13. The basic properties of these models are also given in Table 3. Within the adopted parametrizations, thermohaline mixing produces no significant improvement in the agreement between standard solar models and helioseismic constraints.

4.14 Combined effects of planet engulfment and turbulent mixing

The models presented in Figure 11 already satisfy the principal helioseismic constraints to a high degree. Nevertheless, a small residual

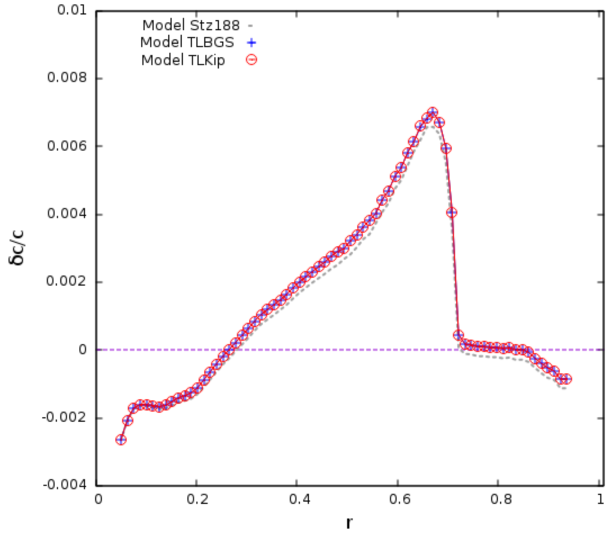

Figure 13. The sound speed difference is plotted with respect to r for the solar models with thermohaline mixing. The cross and circle represent Models TLBGS and TLKip, respectively. Two models are very similar to each other, showing tiny differences compared to Model Sts188 (dark-gray).

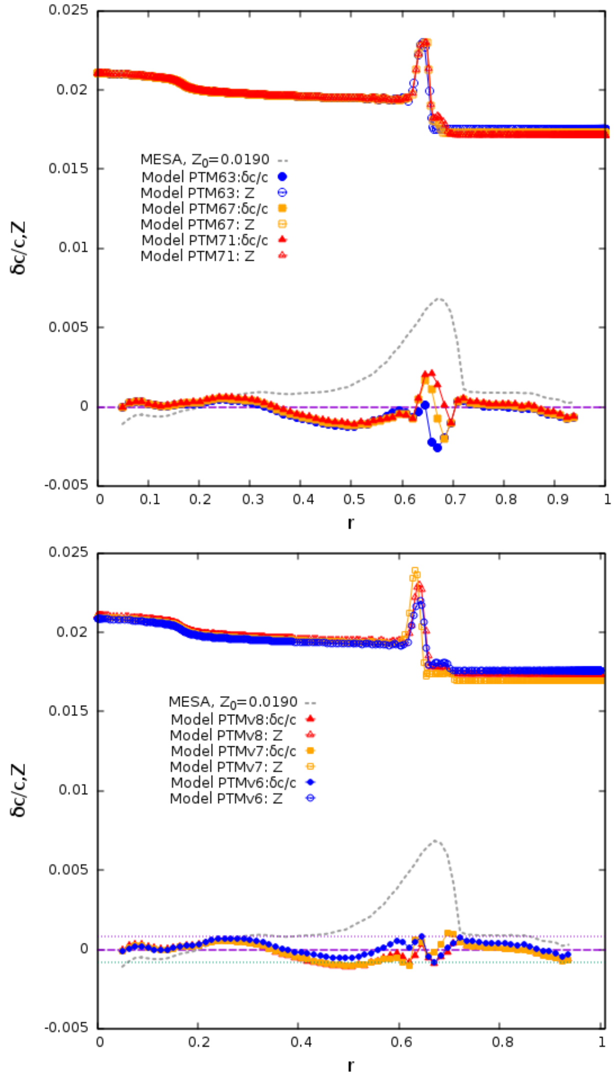

Figure 14. The sound speed difference and metallicity are plotted with respect to r for the solar models with planet engulfment and turbulent mixing. a) Three models are for the different depths of turbulent mixing. $m_{\rm tm}$ of Models PTM63 (circle), PTM67 (square), and PTM71 (triangle) is 0.963, 0.967, and 0.971 $M_\odot$, respectively. b) We obtain the best solar models with variable $m_{\rm tm}$. For Model PTMv6 with Z = 0.0196 (circle), $m_{\rm tm}$ =0.963 $M_\odot$ for age less than 3 Gyr and $m_{\rm tm}$ =0.973 $M_\odot$ for age greater than 3 Gyr. Model PTMv8 (triangle) is similar to Model PTMv6 but its Z = 0.0198. For Model PTMv7 (square) with Z = 0.0198, $m_{\rm tm}$ =0.960 $M_\odot$ for age less than 3 Gyr and $m_{\rm tm}$ =0.975 $M_\odot$ for age greater than 3 Gyr. The upper and lower horizontal dotted lines are for 0.0008 and -0.0008, respectively.

peak in $\delta c/c$ remains immediately beneath the convection zone. Motivated by the possibility that this residual discrepancy originates from turbulent mixing, we investigate models that simultaneously include planetary engulfment and turbulent mixing. Except turbulent mixing process, these models are similar to Models MLTaA and MLTaB. We construct three solar models with three different mixing depths. In Models PTM63, PTM67, and PTM71, turbulent mixing extends down to depth of $m_{\rm tm}$ = 0.963, 0.967, and 0.971 $M_\odot$, respectively. Their sound speed difference and metallicity are plotted with respect to r in Figure 14a. Although the three models have nearly identical global properties, their sound-speed residuals immediately below the convection zone exhibit systematic differences, indicating that the inferred turbulent-mixing depth is tightly constrained by the helioseismic data. It seems that the range of influence of the turbulent mixing extends down to about 0.06 $R_\odot$ below the CZ.

In this case, we can further refine these models by assuming that the depth to which turbulent mixing extends changes with evolution. We construct three solar models with three different Z_0 and variable $m_{\rm tm}$. Z_0 of Models PTMv6, PTMv7, and PTMv8 is 0.0196, 0.0197, and 0.0198, respectively. $m_{\rm tm}$ of Models PTMv6 and PTMv8 is 0.963 for $t < 3$ Gyr and 0.973 for $t > 3$ Gyr. For Model PTMv7, $m_{\rm tm}$ is 0.960 for $t < 3$ Gyr and 0.975 for $t > 3$ Gyr. The sound speed difference and metallicity of these models are plotted with respect to r in Figure 14b. These models provide the best agreement with the complete set of observational constraints obtained in the present study. The $\delta c/c$ difference for Model PTMv6 is less than 0.0008 in the entire solar interior. Very similar differences appear for Models PTMv7 and PTMv8. Their structural parameters are in very good agreement with the helioseismic constraints (Table 2). To our knowledge, these models provide one of the closest simultaneous matches to the observed solar sound-speed profile, convection-zone depth, and surface composition reported in the literature, and the main improvement is achieved with an approach based on planetary engulfment. $M_{\rm p}$ of these models range from 7.2 to 10.5 $M_\oplus$.

A physical motivation for the time-dependent turbulent mixing prescription is that the mass coordinate of the base of the convective zone evolves during stellar evolution. For Model DD1020, the mass coordinate of the convective boundary changes from $\sim$ 0.9705 $M_\odot$ near the zero-age main sequence (0.14 Gyr) to $\sim$ 0.9754 $M_\odot$ at the present solar age. The prefix "DD" in the model names denotes to Dev Dilek, the name adopted here for the hypothetical engulfed planet. The turbulent mixing depth is set to $\sim$ 0.9625 $M_\odot$ before 3 Gyr and $\sim$ 0.9673 $M_\odot$ thereafter.

Expressed in terms of fractional radius, this corresponds to a nearly constant mixing region, at the level of $\sim$ 3.5–3.7% of the solar radius over the entire evolution. This indicates that the apparent transition at

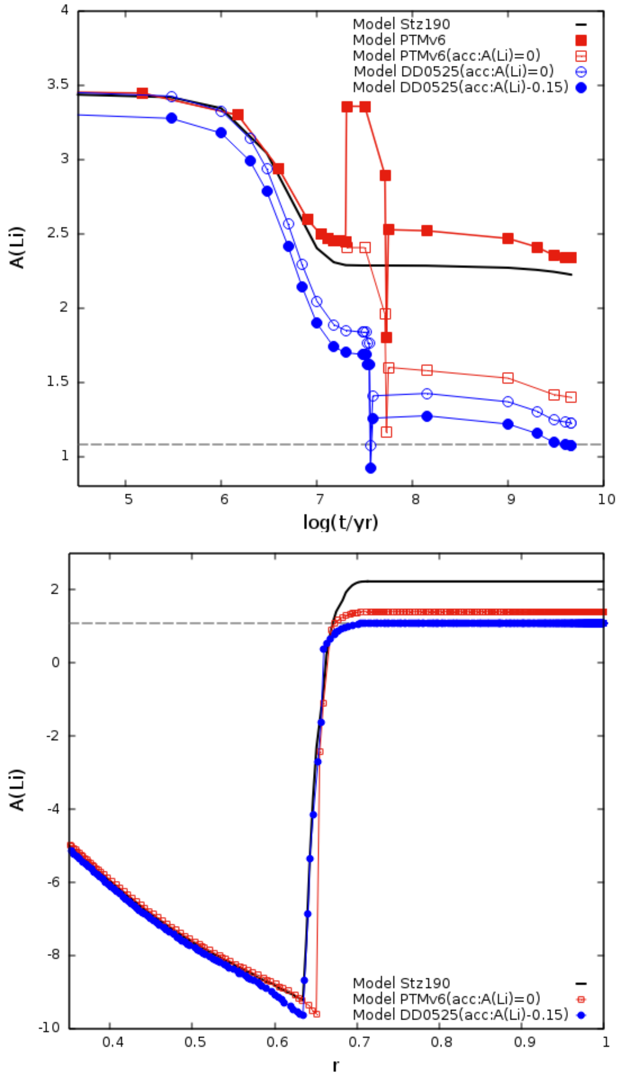

Figure 15. a) Li evolution on the surface of the standard (solid line) and non-standard solar models. The filled square is for Model PTMv6 model when accreted masses have the same Li ratio. A(Li) of these two models is much greater than the observed value (horizontal dotted line). If the accreted matter in Model PTMv6 is Li free (square), then A(Li)=1.40 for the current Sun. The circle shows Model DD0525 (see Section 4.15) with $M_{\rm i}$=0.97 M$_\odot$ and Li-free accretion. A(Li) of this model reduces to 1.22. However, the initial value of A(Li) is about 3.45. We plot also A(Li) − 0.15 for Model DD0525 (filled circle). b) A(Li) of Models Stz190 and PTMv6(acc: A(Li)=9), and A(Li) − 0.15 of Model DD0525 are plotted in the solar interior. The common feature of all three models is the very sharp drop below the CZ.

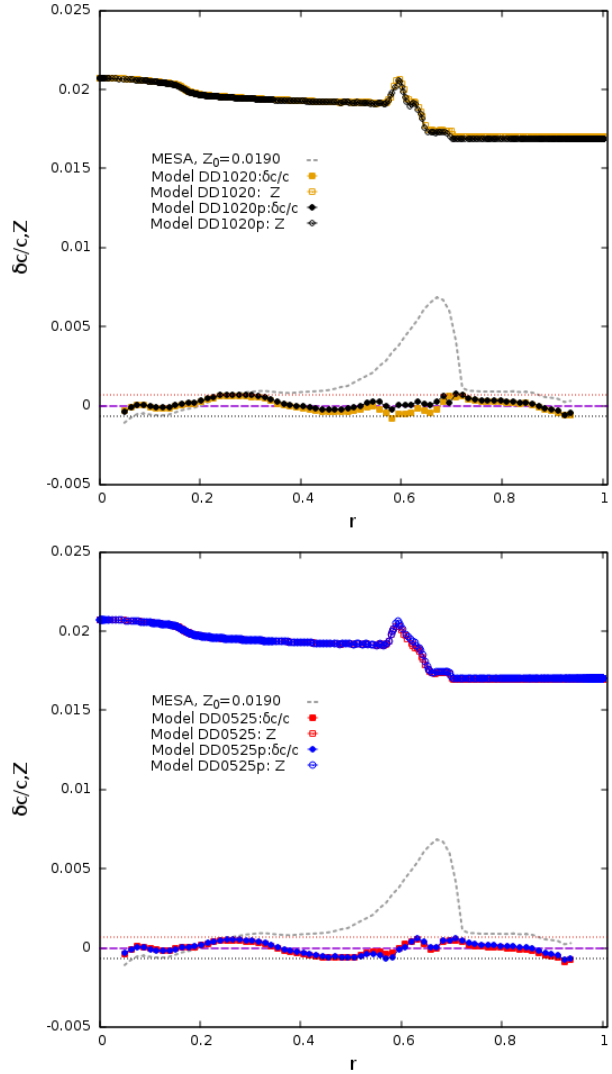

Figure 16. The sound speed difference and metallicity are plotted with respect to r for the solar models with planet engulfment and turbulent mixing. $M_{\rm i}$ of the models is 0.97 M$_\odot$. They are constructed with two mass accretions but without mass loss. a) $M_{\rm acc1}$ and $M_{\rm acc2}$ of the models are 0.01 and 0.02 M$_\odot$, respectively. Z_0 of Models DD1020 (square for Z and filled square for $\delta c/c$) and DD1020p (circle for Z and filled circle for $\delta c/c$) is 0.0195 and 0.019475, respectively. $\delta c/c$ of these models are very similar and less than 0.0007 (dotted horizontal lines). Their $R_{\rm bcz}$s are slightly different (see Table 2). b) $M_{\rm acc1}$ and $M_{\rm acc2}$ of the models are 0.005 and 0.025 M$_\odot$, respectively. Z_0 and $Z_{\rm acc1}$ of both models are 0.0195 and 0.0325, respectively. Their first $t_{\rm acc1}$ and second $t_{\rm acc2}$ accretion times, and $Z_{\rm acc2}$ of the models are slightly different. $Z_{\rm acc2}$ of Models DD0525 (square for Z and filled square for $\delta c/c$) and DD0525p (circle for Z and filled circle for $\delta c/c$) is equal to 0.0155 and 0.0164, respectively.

3 Gyr is primarily a choice of mass coordinate representation rather than a physically distinct change in the mixing structure.

Accordingly, a formulation based on fractional radius would provide a more physically transparent description while yielding nearly identical mixing profiles throughout the solar evolution.

4.15 Non-standard solar models with $M_{\rm i}$=0.97 M$_\odot$ and without mass-loss: the Li depletion in the Sun

Lithium provides one of the most stringent observational constraints on solar evolution models because its surface abundance is highly sensitive to both the early evolution of the solar interior and the chemical composition of any material accreted during the pre-main-sequence and early main-sequence phases. In the planetary-engulfment scenario considered here, the present-day solar lithium abundance therefore offers an independent test of the proposed accretion history. The models therefore allow us to estimate the lithium abundance required in the accreted material to reproduce the observed present-day solar surface abundance, A(Li) ≈ 1.1.

The default MESA composition assumes a lithium-to-metal ratio of $X_{\rm Li}/Z = 7 \times 10^{-7}$. For the standard solar model (Model Stz190), this results in a present-day surface abundance of $A(\rm Li) = 2.22$, substantially larger than the observed value. Figure 15a compares the temporal evolution of the surface lithium abundance for the standard model and several non-standard models. Model PTMv6, in which the accreted material retains the default lithium abundance, yields a similar value, $A(\rm Li) \approx 2.33$. Assuming instead that both accretion episodes are lithium-free reduces the present-day abundance to $A(\rm Li) = 1.40$, demonstrating that the lithium content of the accreted material has a significant influence on the final solar lithium abundance. However, this value still exceeds the observed photospheric abundance.

To investigate whether the lithium constraint can be satisfied simultaneously with the helioseismic constraints, we constructed a new set of models with an initial mass of $M_{\rm i} = 0.97, \rm M_\odot$. These models are closely related to those presented in Section 4.14, but no mass loss is included, and the lower initial mass allows a different redistribution of heavy elements following the two accretion episodes.

We first consider models with $M_{\rm acc1} = 0.01, \rm M_\odot$ and $M_{\rm acc2} = 0.02, \rm M_\odot$. Their principal properties are listed in Table 2. Figure 16a compares the sound-speed difference and metallicity profiles of Model DD1020 with those of Model DD1020p, which differs only by small adjustments to Z_0, $Z_{\rm acc1}$, and $Z_{\rm acc2}$. Both models reproduce the observed solar sound-speed profile remarkably well, with RMS$(\delta c/c)$ below 7×10^{-4}, and provide an excellent match to the depth of the convection zone. Assuming lithium-free accretion, both models yield a present-day surface abundance of $A(\rm Li) \approx 1.25$. Since their initial abundance is $A(\rm Li) \approx 3.45$, adopting an initial solar value lower by approximately 0.15 dex reduces the present-day abundance to the observed level of $A(\rm Li) \approx 1.1$.

As an additional test, we reduced the first accreted mass to $M_{\rm acc1} = 0.005, \rm M_\odot$ while increasing the second accreted mass to $M_{\rm acc2} = 0.025, \rm M_\odot$, producing Models DD0525 and DD0525p. The corresponding sound-speed and metallicity profiles are shown in Figure 16b. Both models remain in excellent agreement with the helioseismic constraints. Model DD0525 reproduces the observed convection-zone depth particularly well, whereas Model DD0525p predicts a slightly deeper convection zone. Their present-day lithium abundances are $A(\rm Li) = 1.22$ and 1.21, respectively. Although this redistribution of the accreted mass slightly improves the agreement with the observed lithium abundance, it still requires the accreted material to be essentially lithium-free.

Figure 15b shows the lithium abundance profiles of the standard solar model (Stz190), Model PTMv6 with lithium-free accretion, and Model DD0525, for which the initial lithium abundance has been reduced by 0.15 dex in order to match the meteoritic value. In all three models the lithium abundance remains nearly constant throughout the convective envelope but decreases abruptly immediately beneath the base of the convection zone, reaching values below $A(\rm Li) \approx -10$. This steep gradient illustrates that lithium depletion is governed by transport into deeper, hotter layers where lithium is efficiently destroyed.

The steep lithium gradient has an important implication for the proposed engulfment scenario. Any additional mixing process introduced to reproduce the observed lithium depletion must remain sufficiently shallow. Otherwise, the localized heavy-element enhancement produced by the engulfed planet (Figure 16) would be redistributed into deeper layers, erasing the metal-rich region responsible for the improved agreement with the helioseismic sound-speed profile. Consequently, the mixing required to explain the solar lithium abundance is constrained not only by the lithium observations themselves but also by the need to preserve the heavy-element enhancement beneath the convection zone.

Table 4. Basic properties of the solar models with different physical assumptions and different numbers of adjustable parameters. The total $\chi^2_{\rm T}$ is defined as $\chi^2_3 + \chi^2_{\rm c}$, where χ^2_3 corresponds to the three global solar constraints ($Z_{\rm s}$, $Y_{\rm s}$, and $R_{\rm bcz}$), and $\chi^2_{\rm c}$ is derived from the sound-speed differences at 71 radial points inside the Sun.

Model	χ^2_3	χ^2_c	$\chi^2_{\rm T}$	k	N	BIC
DD1020	0.162	5065.85	5066.01	10	74	5109.09
PureENGF	0.042	21816.13	21816.17	5	74	21837.71
TurMixaV	47.928	24091.72	24139.65	6	74	24165.49

The relatively narrow range of preferred engulfed planetary masses should therefore not be interpreted as evidence for excessive fine tuning. Instead, it reflects the requirement that several independent observational constraints be satisfied simultaneously, including the helioseismic sound-speed profile, the depth of the convection zone, the surface helium abundance, the surface heavy-element abundance, and the present-day solar lithium abundance. Only a limited region of the multidimensional parameter space satisfies all of these constraints simultaneously within the adopted modelling framework.

For the models with $M_{\rm i} = 0.97, \rm M_\odot$ (DD1020, DD1020p, DD0525, and DD0525p), RMS$(\delta c/c)$ lies in the narrow range 0.00034–0.00036, demonstrating their excellent agreement with the helioseismic inversions. These models consistently favour an engulfed rocky planet with a mass between approximately 4.6 and 5.8 $\rm M_\oplus$, corresponding to the super-Earth regime. The initial planetary mass was likely somewhat larger than the inferred dissolved mass, since part of the planet may survive until reaching the deeper layers of the convection zone before complete disruption. As discussed in Section 6, however, classical aerodynamic drag and ablation alone are unlikely to remove a sufficiently large fraction of the planetary mass during this stage, suggesting that additional physical processes contribute to its final dissolution.

4.16 Statistical comparison of engulfment and non-engulfment models

Model DD1020 (Section 4.15), which combines planetary engulfment with time-dependent turbulent mixing, provides the best overall agreement with the observational constraints considered in this work. The model contains several adjustable parameters: Z_0, $Z_{\rm acc1}$, $Z_{\rm acc2}$, $Y_{\rm acc1}$, $Y_{\rm acc2}$, $t_{\rm acc1}$, $t_{\rm acc2}$, $m_{\rm tm1}$, $m_{\rm tm2}$, and $t_{\rm tm}$. Here, $t_{\rm tm}$ denotes the epoch at which the turbulent-mixing depth changes from $m_{\rm tm1}$ to $m_{\rm tm2}$.

The comparison models were optimized using the same fitting strategy adopted for the engulfment models. The first is an engulfment model without turbulent mixing (Model PureENGF), while the second is a non-engulfment model including turbulent mixing and a time-dependent mixing-length parameter (Model TurMixaV). The control models without engulfment were optimized using the same fitting strategy applied to the engulfment models.

The observational constraints used in this analysis are $Z_{\rm s}$, $Y_{\rm s}$, $R_{\rm bcz}$, and the sound speed evaluated at 71 radial points inside the Sun. The standard solar calibration constraints associated with the present-day solar luminosity ($\rm L_\odot$) and radius ($\rm R_\odot$) are not included in the parameter-counting analysis discussed below. In standard solar modelling, these two constraints are conventionally satisfied by adjusting the initial helium abundance (Y_0) and the mixing-length parameter (α). Since these calibration parameters are required for all solar mod-

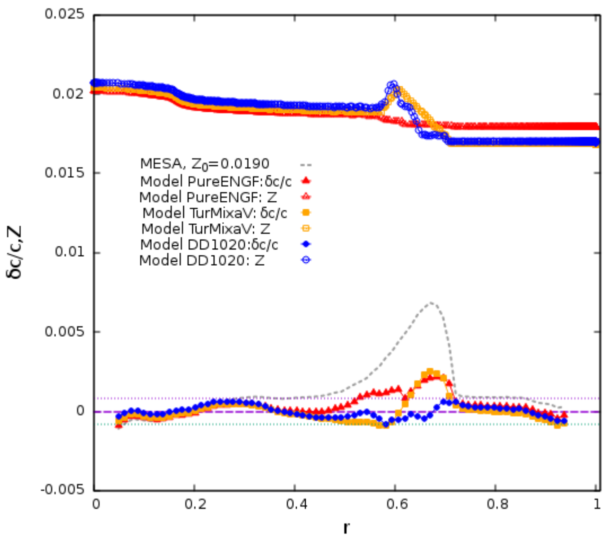

Figure 17. The sound-speed difference and metallicity are plotted as functions of r for the solar models with planetary engulfment (Model PureENGF, triangles) and with turbulent mixing plus variable α (Model TurMixaV, squares). For comparison, Model DD1020 (circles) and the standard solar model with $Z_0 = 0.0190$ (gray curve) are also shown. Filled symbols represent $\delta c/c$, while open symbols represent Z. Model DD1020 exhibits the smallest sound-speed deviations and therefore the lowest χ_c^2. Although the turbulent-mixing and variable-α model partially improves the sound-speed agreement relative to standard solar models, it does not reproduce the same overall agreement achieved by the engulfment models. In addition, the surface metallicity of Model TurMixaV exceeds the observationally inferred value.

els, including standard models, they are not treated here as additional free parameters specific to the engulfment or non-standard scenarios.

The number of adjustable parameters is taken to be $k = 5$ for Model PureENGF (Z_0, $Z_{\rm acc1}$, $Y_{\rm acc}$, $t_{\rm acc}$, and $M_{\rm acc1}$). In this model, $Y_{\rm acc1} = Y_{\rm acc2}$, and the two accretion episodes occur consecutively. For Model TurMixaV, the number of adjustable parameters is $k = 6$ ($Z_0, \alpha_1, t_1, m_{\rm tm1}, m_{\rm tm2}$, and $t_{\rm tm}$), where α_1 is the value of α for $t < t_1$.

To assess whether the improved agreement of the engulfment models could arise solely from increased model flexibility, we compute the Bayesian Information Criterion (BIC):

$$BIC = \chi^2_{\rm T} + k\ln(N), \quad (6)$$

where N is the number of observational constraints and k is the number of adjustable parameters (Schwarz 1978; Liddle 2007). The total χ^2 is defined as

$$\chi^2_{\rm T} = \chi^2_3 + \chi^2_c, \quad (7)$$

with

$$\chi^2_3 = \sum_{i=1}^{3}\left(\frac{f_{i\rm obs} - f_{i\rm mod}}{\sigma_{i\rm obs}}\right)^2, \quad (8)$$

and

$$\chi^2_c = \sum_{i=1}^{71}\left(\frac{c_{i\rm obs} - c_{i\rm mod}}{\sigma_{ic\rm obs}}\right)^2. \quad (9)$$

Here, $\sigma_{i\rm obs}$ and $\sigma_{ic\rm obs}$ denote the uncertainties associated with the three global observables and the sound-speed profile, respectively.

The basic properties of the models are summarized in Table 4. Figure 17 compares the sound-speed differences and metallicity profiles of the three models. Model DD1020 yields the best overall agreement with the helioseismic constraints and has the smallest χ_c^2.

The absolute χ_c^2 values remain relatively large for all models because the observational uncertainties in the helioseismically inferred sound speed are extremely small. As a result, even modest residual differences between the models and the observed sound-speed profile contribute significantly to the total χ_c^2, particularly in the region $0.2, {\rm R}_\odot \lesssim r \lesssim 0.7, {\rm R}_\odot$. The comparison between models is therefore more meaningful in a relative sense, namely through differences in χ_c^2 and BIC values obtained using the same observational constraints and fitting procedure.

Although Model TurMixaV improves the agreement relative to standard solar models, its sound-speed residuals remain substantially larger than those of the engulfment models, particularly in the region below the convective zone.

The BIC comparison indicates that the superior agreement achieved by the engulfment models cannot be attributed solely to the increased number of adjustable parameters. Despite containing more free parameters, Model DD1020 remains strongly favoured over the optimized non-engulfment model TurMixaV. Similarly, Model PureENGF yields substantially lower BIC values than Model TurMixaV, indicating that planetary engulfment provides the dominant improvement in reproducing the helioseismic constraints among the physical ingredients examined in this study.

5 DISCUSSION

5.1 Can we call metal-rich accretion a planetary engulfment?

Symbolically, our scenario consists of two distinct accretion episodes: an initial metal-rich accretion followed by a metal-poor accretion phase. Chemical fractionation naturally occurs in protoplanetary discs during planet formation. As refractory elements become incorporated into planetary bodies, the remaining gas becomes relatively depleted in heavy elements. Part of this metal-poor gas may subsequently be accreted by the host star, while part may be dispersed from the system. Within this framework, the metal-rich accretion is interpreted as the signature of planetary engulfment. Furthermore, theoretical studies of planet engulfment indicate that engulfed planetary material can penetrate beneath the convective envelope before becoming mixed into the stellar interior.

In the radiative interior of a solar-type star, where nuclear reactions do not modify the abundances of heavy elements, the formation of a localized enhancement in metallicity is difficult to achieve through standard stellar evolution alone. Convective mixing, semiconvective transport, and microscopic diffusion all tend to smooth abundance gradients rather than create localized peaks. Consequently, a metal-rich layer immediately beneath the convection zone is more naturally explained by an external source of heavy elements, such as planetary engulfment.

5.2 Z-bump and other effects for model improvement

It has long been recognized that solar models computed with the GS98 and GN93 abundance mixtures are generally in better agreement with helioseismic observations than models based on more recent low-metallicity abundance determinations (Bahcall, Serenelli, & Pinsonneault 2004). Consistent with this trend, the engulfed planetary masses inferred for the low-metallicity solar models presented in Table 2 are systematically larger than those obtained for the high-metallicity models. Our calculations further show that, regardless of the adopted opacity tables, equation of state, solar composition, turbulent or thermohaline mixing prescription, or time-dependent mixing-length parameter, introducing a localized metallicity enhancement beneath the convection zone consistently improves the agreement between solar models and helioseismic observations. Although several internal transport processes (such as rotationally induced mixing or transient convective instabilities) may alter the chemical stratification beneath the convection zone, none of them naturally produces a localized metal-rich layer. If such a metallicity enhancement exists, an external origin, such as planetary engulfment, provides a plausible explanation.

Opacity enhancement has also been proposed as a possible solution to the solar modelling problem. In opacity-based approaches, the required opacity increase is inferred directly from the discrepancies between models and observations. In contrast, the planetary-engulfment scenario predicts a physical quantity—the engulfed planetary mass—that can be estimated directly from the stellar models. Moreover, the inferred planetary masses can be compared with the observed distribution of exoplanet masses, providing an additional observational consistency check that is not available in purely opacity-based solutions.

The required opacity enhancement is calculated entirely from the model. However, we not only calculate the minimum required planetary mass from the model but also find clues from the planetary mass and a distribution (see below).

Rotation and angular-momentum evolution also introduce additional mixing processes through a variety of hydrodynamic instabilities. Since the young Sun rotated substantially faster than at present, rotationally induced mixing may have modified the present-day chemical stratification beneath the convection zone (Christensen-Dalsgaard 2021).

5.3 Further evidence for planet engulfment in planetary mass distributions

Figure 18a shows the planetary masses listed in TEPCat (Southworth 2011) as a function of orbital semi-major axis. Only planets with mass uncertainties smaller than 20% are included. The shaded regions indicate the parameter space where planets are expected to be engulfed during different stages of stellar evolution according to De et al. (2023). The orange region corresponds to engulfment before the red-giant phase ($R < 4$ R$_\odot$), whereas the red region corresponds to engulfment during the red-giant phase ($4 < R < 50$ R$_\odot$).

The planetary-mass histogram shown in Figure 18b exhibits several prominent features. The dominant peak occurs near 1 M$_\mathrm{J}$, while a second concentration is found in the range 0.01–0.03 M$_\mathrm{J}$. Massive planets and brown dwarfs are primarily distributed between approximately 50 and 83 M$_\mathrm{J}$. Between these two populations lies the well-known brown-dwarf desert. Another apparent deficit is present around 0.1 M$_\mathrm{J}$. The observed distribution is shaped by both the formation and subsequent dynamical evolution of planetary systems, as well as by observational selection effects. An interesting question is whether part of the apparent scarcity of planets near 0.1 M$_\mathrm{J}$ could also be related to planetary engulfment.

While planet engulfment offers a plausible explanation for the apparent paucity of planets in the mass range around 0.1 M_J, it is not the only mechanism that has been proposed. Alternative explanations include orbital migration processes that relocate such planets to smaller separations or remove them from the observed population, formation pathways that intrinsically produce fewer planets in this mass regime, and post-formation mass loss through mechanisms such as photoevaporation or irradiation-driven atmospheric escape. These processes may operate concurrently, and disentangling their relative contributions remains an open problem. In the present work, we focus specifically on the engulfment hypothesis and evaluate whether it provides a self-consistent explanation for the helioseismic structure of the Sun together with its observed surface chemical composition.

The apparent scarcity of planets at very small orbital separations ($a < 0.045$ AU) is particularly noticeable near $\log(M_\mathrm{p}/M_\mathrm{J}) \approx -0.5$, -1.3, and around the Neptune-mass regime (vertical red dotted line in the inset of Figure 18b). The deficit near Neptune masses spans a relatively narrow interval (0.7–1.1 M$_\mathrm{N}$), whereas the higher-mass deficit extends over a much broader range (1–10 M$_\mathrm{J}$), producing a triangular region of comparatively low planet occurrence. We emphasize, however, that the existence and depth of these apparent gaps—especially in the Neptune-mass regime—are strongly affected by observational selection effects. Radial-velocity and transit surveys have reduced completeness for close-in intermediate-mass planets owing to instrumental sensitivity, stellar activity, and survey selection biases. Consequently, the observed deficit should not be interpreted as direct evidence for planetary engulfment, although it is qualitatively consistent with such a scenario.

6 PHYSICAL CONSTRAINTS ON PLANET SURVIVAL

6.1 Roche-lobe stability of engulfed planets

Planetary engulfment has been proposed as a potentially important process affecting the evolution, surface composition, and internal structure of stars (Sandquist et al. 2002; Metzger, Giannios & Spiegel 2012; Jia & Spruit 2017, 2018). A fundamental question in such scenarios is whether a close-in planet can survive its final approach to the stellar surface without being catastrophically disrupted by Roche-lobe overflow. If the planetary radius substantially exceeds its Roche-lobe radius (R_RL), significant mass loss is expected before the planet enters the stellar envelope, thereby limiting the amount of heavy elements transported into the stellar interior. We therefore begin by examining the Roche-lobe stability of compact rocky planets at the surface of our best-fitting solar model.

The Roche-lobe radius was calculated using the analytical approximation derived by Eggleton (1983),

$$R_\mathrm{RL} = \frac{0.49q^{2/3}}{0.6q^{2/3} + \ln(1 + q^{1/3})}a, \qquad (10)$$

where ($q = M_\mathrm{p}/M_\star$), M_p is the planetary mass, $M_\star$ is the stellar mass. Throughout this section, the Roche-lobe radius is evaluated at the surface of the DD1020 pre-main-sequence solar model, adopting $M = 0.97$ M$_\odot$ and $R = 0.924$ R$_\odot$.

Figure 19 compares the Roche-lobe radius with the observed radii of super-Earths and Neptune-like planets taken from the TEPCat catalogue (Southworth 2011), together with the radii of our core-dominated rocky planet models computed using the MAGRATHEA planetary interior structure code (Huang, Rice, & Steffen 2022). In the present work, we adopted $q_\mathrm{c} = M_\mathrm{core}/M_\mathrm{p} = 1$, corresponding to fully differentiated rocky planets, because the engulfment scenario investigated here concerns compact rocky bodies rather than volatile-rich planets. The observed super-Earths and Neptune-like planets generally possess radii substantially larger than their corresponding Roche-lobe radii, implying that planets retaining significant volatile envelopes are expected to undergo extensive Roche-lobe overflow before entering the stellar envelope.

In contrast, the radii of the core-dominated planetary models ($q_\mathrm{c} = 1$) are remarkably close to the Roche-lobe radius over a wide

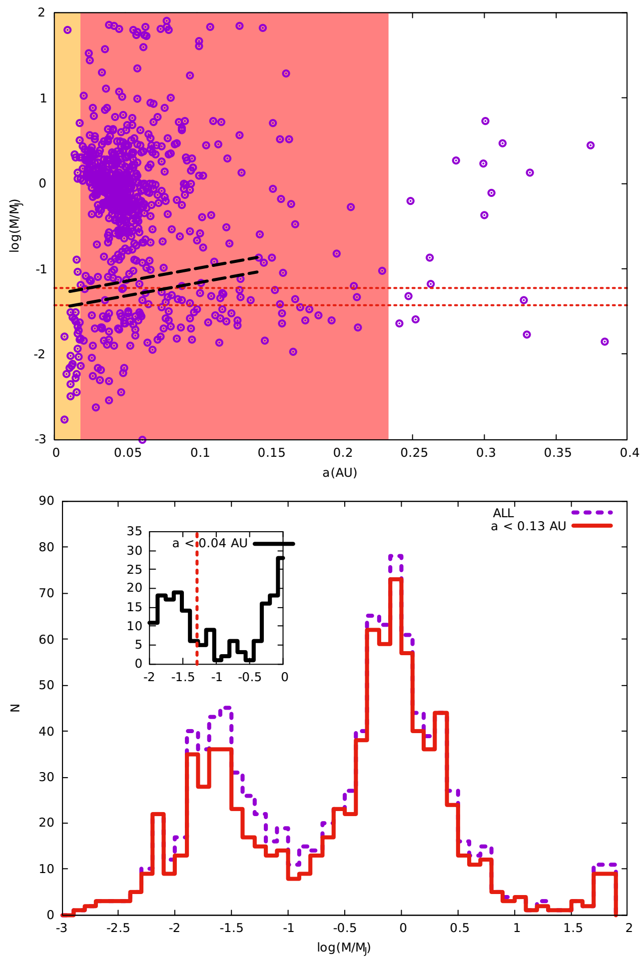

Figure 18. Mass versus semi-major axis and histogram for the planetary mass. (*a*) Mass is plotted with respect to the semi-major axis. The horizontal red dotted lines correspond M_p=0.7 and 1.1 $\mathrm{M_N}$. The black dashed lines define the area where almost no Neptune-like planets are observed. (*b*) Histogram of planetary masses for the comparison sample, showing the number of detected planets as a function of planetary mass (solid line). The dotted lines show the histogram for the planets with $a < 0.13$ AU. Two data samples show a similar distribution. The inset shows histogram for the planets with $a < 0.04$ AU and mass range $-2 < \log(M_\mathrm{p}/\mathrm{M_J}) = -0.5 < 0$. When we look at the planets closest to the host, we see more minima in the histogram. This pattern is likely a result of engulfment. The vertical red dotted line in the inset marks the mass of the dissolved planet for Model N.

range of planetary masses. The agreement is particularly notable because the Roche-lobe radius is determined solely by the stellar and planetary masses, whereas the planetary radii were obtained independently from detailed interior models. This comparison indicates that compact rocky planets, or the stripped cores of initially Neptune-like planets, may approach the stellar surface without experiencing catastrophic tidal disruption.

It should be emphasized that the present Roche-lobe analysis is applicable only up to the moment when the planet reaches the stellar surface. Once the planet enters the convective envelope, the Roche geometry is no longer well defined and the subsequent evolution is governed by the local stellar environment. In particular, the increasing pressure and density of the stellar envelope modify the planetary structure and determine the efficiency of drag and aerodynamic ablation. These processes are investigated in the following subsections.

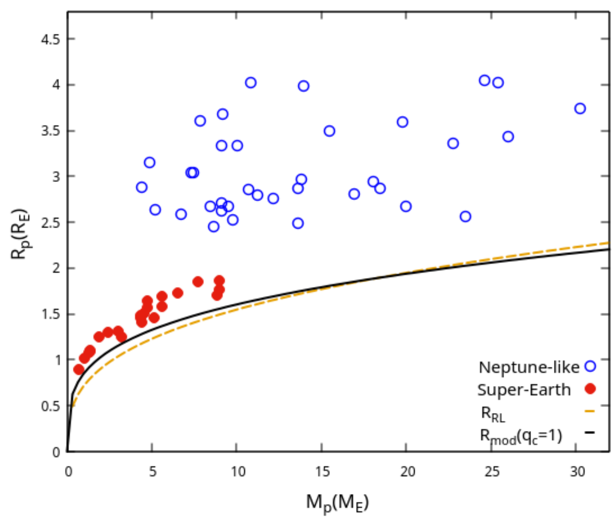

Figure 19. Planetary radius as a function of planetary mass. Filled circles represent observed super-Earths, while open circles denote Neptune-like planets from the TEPCat catalogue. The dashed curve shows the Roche-lobe radius, R_RL, calculated at the surface of the DD1020 pre-main-sequence solar model ($M_\star$ = 0.97 $\mathrm{M_\odot}$, $R_\star$ = 0.924 $\mathrm{R_\odot}$). The solid curve gives the radii of core-dominated rocky planets ($q_\mathrm{c} = M_\mathrm{core}/M_\mathrm{p} = 1$) obtained from our MAGRATHEA interior models. Whereas the observed radii of both super-Earths and Neptune-like planets generally exceed their corresponding Roche-lobe radii, the compact core-dominated models closely follow the Roche-lobe limit over a broad range of planetary masses. This result suggests that rocky planets that have lost most or all of their volatile envelopes may enter the stellar envelope without experiencing catastrophic Roche-lobe overflow.

6.2 Structural response of engulfed rocky planets to the stellar envelope

Once a planet penetrates the stellar surface, the Roche geometry is no longer applicable and the subsequent evolution is governed by the physical conditions within the stellar envelope. In particular, the ambient pressure and density increase rapidly with depth, modifying both the planetary structure and its interaction with the surrounding stellar material. These quantities therefore provide the essential input for evaluating drag forces and aerodynamic ablation during the engulfment process.

The upper panel of Figure 20 shows the pressure and density profiles throughout the convective envelope of Model DD1020. Analytical fitting functions were derived for both quantities and subsequently adopted in the calculations presented below. Between the stellar surface and the base of the convective envelope, the gas pressure increases by nearly nine orders of magnitude, while the density rises by more than six orders of magnitude. Such extreme variations are expected to have a significant influence on the structure of an engulfed rocky planet.

To quantify this effect, we computed a new grid of planetary interior models (Yıldız & Örtel 2026 in preparation) using the MAGRATHEA code (Huang, Rice, & Steffen 2022). Core-dominated rocky planets with masses of 6, 8 and 10 $\mathrm{M_\oplus}$ were calculated over a wide range of external pressures corresponding to those encountered within the convective envelope of Model DD1020, while keeping the surface temperature fixed at 3000K. The resulting pressure-dependent planetary radii were then combined with the stellar pressure profile to obtain the variation of planetary radius as a function of depth.

The lower panel of Figure 20 presents the normalized planetary radius, $R_{\rm p}(P(r))/R_{\rm p,s}$, where $R_{\rm p,s}$ denotes the planetary radius at the stellar surface. All three planetary models undergo progressive compression as they move deeper into the convective envelope. For the 10 $M_\oplus$ model, the radius decreases by approximately 26 per cent between the stellar surface and the base of the convective envelope, while the reduction reaches about 29 per cent for the 6 $M_\oplus$ model. The larger compression experienced by the lower-mass planets reflects their lower mean densities and weaker resistance to external pressure.

The reduction in planetary radius has important consequences for the subsequent dynamical evolution. Since both the aerodynamic drag force and the classical ablation rate depend directly on the planetary cross-sectional area, $A = \pi R_{\rm p}^2$, pressure-induced compression continuously reduces the effective interaction area as the planet penetrates the stellar envelope. Consequently, neglecting the structural response of the planet would systematically overestimate both the drag force and the associated mass-loss rate.

The present calculations consider only the mechanical effect of the increasing external pressure. Thermal expansion caused by frictional heating, shocks, and heat exchange with the surrounding stellar plasma has not been included because self-consistent high-temperature planetary models are presently unavailable. The pressure-induced contraction derived here should therefore be regarded as a lower limit to the planetary radius under engulfment conditions. The influence of thermal effects on planetary survival will require dedicated future modelling.

6.3 Classical drag and aerodynamic ablation

Having established that compact rocky planets can survive the Roche-lobe constraint and that their radii decrease owing to compression within the stellar envelope, we now estimate the effects of aerodynamic drag and classical ablation during the subsequent inward motion of the planet.

The ram pressure exerted by the surrounding stellar material is

$$\frac{1}{2}\rho v^2, \tag{11}$$

where ρ is the local density of the stellar envelope and v is the velocity of the planet relative to the surrounding gas.

The corresponding drag force is

$$\frac{1}{2}C_{\rm D}\rho v^2 A, \tag{12}$$

where $C_{\rm D}$ is the drag coefficient and

$$\pi R_{\rm p}^2, \tag{13}$$

is the instantaneous cross-sectional area of the planet. Since the planetary radius decreases with increasing external pressure (Section 6.2), the drag force varies not only because of the rapidly increasing stellar density but also because of the progressive compression of the planet.

The classical aerodynamic ablation rate is estimated from the balance between the kinetic energy intercepted by the planet and the energy required to remove planetary material,

$$\frac{C_{\rm H}}{Q}F_{\rm D}v, \tag{14}$$

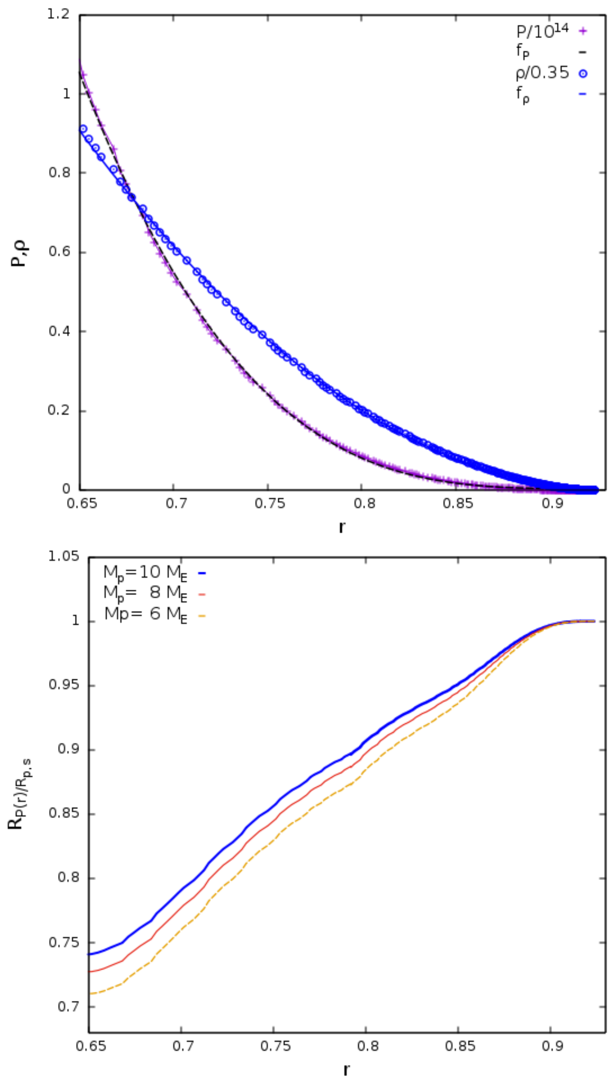

Figure 20. a) (a) Pressure (P) and density (ρ) profiles in the convective envelope of Model DD1020 as functions of fractional radius. For clarity, P (crosses) and ρ (circles) are normalized by 10^{14} dyn cm^{-2} and 0.35 g cm^{-3}, respectively. The solid and dashed curves represent the analytical fitting functions adopted for $\rho(r)$ and $P(r)$. b) Relative planetary radius, $R_{\rm p}(P(r))/R_{\rm p,s}$, as a function of radius for core-dominated rocky planets with masses of 6, 8 and 10 $M_\oplus$, where $R_{\rm p,s}$ is the planetary radius at the stellar surface. The curves were obtained from the pressure-dependent MAGRATHEA interior models assuming no thermal expansion.

where $C_{\rm H}$ is the heat-transfer coefficient and Q is the effective specific energy required to remove unit mass from the planet.

The adopted parameters for the reference calculation are summarized in Table 5. Throughout this section we adopt $C_{\rm D} = 1$, $C_{\rm H} = 0.05$, and $Q = 3 \times 10^{11}$ erg/g. The planetary cross-sectional area is evaluated using the pressure-dependent planetary radius obtained from the MAGRATHEA models described in Section 6.2. As a first-order approximation, the planetary velocity is assumed to remain constant at 447 km/s during the passage through the convective envelope. Although the actual velocity is expected to evolve under the combined effects of gravity and drag, the constant-velocity approximation provides a useful reference model for evaluating the efficiency of classical aerodynamic ablation.

Table 5. Parameters adopted for the reference aerodynamic drag and ablation calculation.

Parameter	Value
Planet mass, M_p	10 $M_\oplus$
Initial velocity, v_0	447 km/s
Drag coefficient, C_D	1.0
Heat-transfer coefficient, C_H	0.05
Specific ablation energy, Q	3×10^{11} erg/g
Planetary radius	$R_p(P)$ from MAGRATHEA models
Stellar model	DD1020

For the reference model, the calculated mass loss is negligible compared with the initial planetary mass. Despite the rapid increase in the density of the stellar envelope with depth, the planet traverses the convective envelope on a timescale of only a few hours, leaving insufficient time for significant aerodynamic erosion. Furthermore, the pressure-induced reduction in planetary radius continuously decreases the effective cross-sectional area, thereby reducing both the drag force and the ablation rate.

It should be emphasized that the adopted parameter values are deliberately conservative in the sense that they maximize the efficiency of classical aerodynamic erosion. Even under these assumptions, classical drag and ablation remove only a negligible fraction of the planetary mass before the planet reaches the base of the convective envelope. Consequently, classical aerodynamic ablation alone cannot account for the dissolution of several Earth masses of rocky material during the engulfment process.

It should be emphasized that the adopted parameter values were intentionally chosen to favour aerodynamic mass loss. Specifically, we adopted a relatively large heat-transfer coefficient ($C_H = 0.05$), a standard drag coefficient ($C_D = 1$), and a comparatively low specific ablation energy ($Q = 3 \times 10^{11}$ erg/g), all of which maximize the efficiency of classical aerodynamic erosion. Even under these conservative assumptions, the calculated mass loss remains negligible compared with the initial planetary mass, indicating that classical drag and ablation alone cannot disrupt a compact rocky planet before it reaches the base of the solar convective envelope.

The present calculation intentionally isolates the contribution of classical aerodynamic ablation. Although additional processes, including fragmentation, shocks, thermal expansion, hydrodynamic instabilities, and dissolution in the deeper stellar envelope, may substantially modify the subsequent evolution, our calculations demonstrate that classical drag and ablation alone cannot destroy a compact rocky planet during its passage through the solar convective envelope. The engulfment scenario proposed for Model DD1020 therefore remains physically plausible. A fully self-consistent hydrodynamic treatment including orbital evolution and planetary dissolution is beyond the scope of the present study and is left for future work.

7 CONCLUSIONS

This study demonstrates that early planetary engulfment provides a physically and observationally consistent framework for resolving several long-standing discrepancies between standard solar models and helioseismic observations. Solar models incorporating mass accretion and chemical restructuring are able to reproduce helioseismic constraints, the depth of the convective-zone base, and surface abundance measurements with substantially improved agreement. Among the explored models, Model DD1020 yields the best overall consistency with observational data, combining planetary engulfment with turbulent mixing and achieving the lowest combined misfit to both helioseismic and photospheric constraints.

A key result of this work is that the inferred improvements are not solely a consequence of increased model flexibility. Optimized control models incorporating turbulent mixing and variable mixing-length prescriptions partially improve upon standard solar models, but they do not reproduce the same level of agreement achieved by the engulfment-based models. A model-complexity assessment using information-criterion arguments further indicates that the superior performance of the engulfment models cannot be explained solely by their larger number of adjustable parameters.

The preferred solution, Model DD1020, implies the engulfment of Dev Dilek, a super-Earth–mass planet with $M \simeq 5.6\ M_\oplus$ ($\simeq 0.33\ M_N$). Closely related best-fit solutions across the model set consistently favour engulfed planetary masses in the range $\sim$ 5–10 $M_\oplus$, suggesting a robust preference for a super-Earth regime. In all cases, the engulfed material is transported below the convective zone ($m \simeq 0.96$–$0.973\ M_\odot$), where it produces a localized enhancement of heavy elements that modifies the internal opacity and stratification.

Lithium depletion can also be reproduced within this framework, provided that the accreted material is lithium-poor and that additional mixing beneath the convection zone remains sufficiently limited to preserve the heavy-element enhancement required by the helioseismic constraints.

An additional outcome of this work is the first-order physical assessment of the planet-engulfment scenario presented in Section 6. By combining Roche-lobe stability, high-pressure planetary interior models computed with MAGRATHEA, and classical aerodynamic drag and ablation, we examined whether a compact rocky planet can survive its passage through the solar convective envelope. The calculations show that core-dominated rocky planets remain close to their Roche-lobe radii at the stellar surface and undergo progressive compression as they descend through the convective envelope. Although the increasing stellar density enhances the aerodynamic drag, the pressure-induced reduction in planetary radius decreases the effective cross-sectional area and consequently suppresses both the drag force and the classical ablation rate. Even under conservative assumptions chosen to maximize aerodynamic erosion, the predicted mass loss remains negligible compared with the planetary mass. These results therefore indicate that classical aerodynamic drag and ablation alone are insufficient to disrupt a compact rocky planet before it reaches the base of the solar convective envelope.

Taken together, the results presented in this work strengthen the physical plausibility of the proposed planet-engulfment scenario. Within the explored modelling framework, planetary engulfment provides a unified explanation for the principal discrepancies between standard solar models and helioseismic constraints while remaining consistent with current observational evidence. At the same time, the present analysis demonstrates that a complete description of the engulfment process requires a fully coupled treatment of orbital dynamics, planetary structural evolution, thermal effects, shock formation, and hydrodynamic instabilities. If confirmed by future theoretical and observational studies, planetary engulfment may represent a key missing ingredient in the construction of realistic solar and stellar models. The results presented here suggest that planetary engulfment should be considered in stellar evolution calculations for stars hosting planetary systems, particularly when precise asteroseismic constraints are available.

ACKNOWLEDGEMENTS

It is a great pleasure to obtain a solar model that is in very good agreement with the observations. This success is also the success of very advanced observational data and theoretical results. Many thanks to all these efforts and to the team that created the MESA stellar evolution code, which is constantly updated and improved. The author acknowledges Dr. Tansel Ak for his very fruitful discussions on the paper. This work is supported by the Scientific and Technological Research Council of Turkey (TÜBİTAK: 122F107).

CORRESPONDENCE

Correspondence and requests for materials should be addressed to M.Y. (email: mutlu.yildiz@ege.edu.tr).

DATA AVAILABILITY

The data underlying this article will be shared on reasonable request to the corresponding author. The solar models are constructed using the MESA v15140 version. The inlists of Models DD0525 and PTMv6, and the fgong files can be found on Github.

CODE AVAILABILITY

The asteroseismic modeling was performed using MESA. (https://docs.mesastar.org).

REFERENCES

Angulo C., Arnould M., Rayet M., Descouvemont P., Baye D., Leclercq-Willain C., Coc A., et al., 1999, NuPhA, 656, 3. doi:10.1016/S0375-9474(99)00030-5

Asplund M., Grevesse N., Sauval A. J., Scott P., 2009, ARA&A, 47, 481. doi:10.1146/annurev.astro.46.060407.145222

Bahcall J. N., Serenelli A. M., Pinsonneault M., 2004, ApJ, 614, 464. doi:10.1086/423027

Bahcall J. N., Pinsonneault M. H., 2004, PhRvL, 92, 121301. doi:10.1103/PhysRevLett.92.121301

Baraffe, I., Chabrier, G., & Gallardo, J. 2010, ApJ, 702, L27

Basu S., Antia H. M., 1995, MNRAS, 276, 1402. doi:10.1093/mnras/276.4.1402

Basu S., Antia H. M., 1997, MNRAS, 287, 189. doi:10.1093/mnras/287.1.189

Basu S., Christensen-Dalsgaard J., Chaplin W. J., Elsworth Y., Isaak G. R., New R., Schou J., et al., 1997, MNRAS, 292, 243. doi:10.1093/mnras/292.2.243

Brown J. M., Garaud P., Stellmach S., 2013, ApJ, 768, 34. doi:10.1088/0004-637X/768/1/34

Brun A. S., Antia H. M., Chitre S. M., Zahn J.-P., 2002, A&A, 391, 725. doi:10.1051/0004-6361:20020837

Beccari G., De Marchi G., Panagia N., Valenti E., Carraro G., Romaniello M., Zoccali M., et al., 2015, A&A, 574, A44. doi:10.1051/0004-6361/201424077

Bedell M., Bean J. L., Meléndez J., Spina L., Ramírez I., Asplund M., Alves-Brito A., et al., 2018, ApJ, 865, 68. doi:10.3847/1538-4357/aad908

Behmard A., Dai F., Brewer J. M., Berger T. A., Howard A. W., 2023, MNRAS, 521, 2969. doi:10.1093/mnras/stad745

Böhm-Vitense E., 1958, ZA, 46, 108

Brun A. S., Antia H. M., Chitre S. M., Zahn J.-P., 2002, A&A, 391, 725. doi:10.1051/0004-6361:20020837

Buldgen G., Pain J.-C., Cossé P., Blancard C., Gilleron F., Pradhan A. K., Fontes C. J., et al., 2025, NatCo, 16, 693. doi:10.1038/s41467-024-54793-y

Castro M., Vauclair S., Richard O., 2007, A&A, 463, 755. doi:10.1051/0004-6361:20066327

Caughlan G. R., Fowler W. A., 1988, ADNDT, 40, 283. doi:10.1016/0092-640X(88)90009-5

Charbonnel C., Zahn J.-P., 2007, A&A, 467, L15. doi:10.1051/0004-6361:20077274

Christensen-Dalsgaard J., Däppen W., Ajukov S. V., et al., 1996, Science, 272, 1286

Christensen-Dalsgaard J., 2021, LRSP, 18, 2. doi:10.1007/s41116-020-00028-3

Church R. P., Mustill A. J., Liu F., 2020, MNRAS, 491, 2391. doi:10.1093/mnras/stz3169

Cyburt R. H., Amthor A. M., Ferguson R., Meisel Z., Smith K., Warren S., Heger A., et al., 2010, ApJS, 189, 240. doi:10.1088/0067-0049/189/1/240

De K., MacLeod M., Karambelkar V., Jencson J. E., Chakrabarty D., Conroy C., Dekany R., et al., 2023, Natur, 617, 55. doi:10.1038/s41586-023-05842-x

Denissenkov P. A., Merryfield W. J., 2011, ApJL, 727, L8. doi:10.1088/2041-8205/727/1/L8

Desch S. J., 2007, ApJ, 671, 878. doi:10.1086/522825

Eggleton P. P., 1983, ApJ, 268, 368. doi:10.1086/160960

Ezer D., Cameron A. G. W., 1965, CaJPh, 43, 1497. doi:10.1139/p65-140

Gonzalez G., 1997, MNRAS, 285, 403. doi:10.1093/mnras/285.2.403

Grevesse N., Sauval A. J., 1998, SSRv, 85, 161. doi:10.1023/A:1005161325181

Guzik J. A., Watson L. S., Cox A. N., 2005, ApJ, 627, 1049. doi:10.1086/430438

Guzik J. A., Mussack K., 2010, ApJ, 713, 1108. doi:10.1088/0004-637X/713/2/1108

Hartigan P., Edwards S., Ghandour L., 1995, ApJ, 452, 736. doi:10.1086/176344

Hartmann L., Herczeg G., Calvet N., 2016, ARA&A, 54, 135. doi:10.1146/annurev-astro-081915-023347

Herczeg G. J., Dong S., Shappee B. J., Chen P., Hillenbrand L. A., Jose J., Kochanek C. S., et al., 2016, ApJ, 831, 133. doi:10.3847/0004-637X/831/2/133

Hon M., Huber D., Rui N. Z., Fuller J., Veras D., Kuszlewicz J. S., Kochukhov O., et al., 2023, Nature, 618, 917. doi:10.1038/s41586-023-06029-0

Huang C., Rice D. R., Steffen J. H., 2022, MNRAS, 513, 5256. doi:10.1093/mnras/stac1133

Iglesias C. A., Rogers F. J., 1996, ApJ, 464, 943. doi:10.1086/177381

Irwin A. W., 2012, ascl.soft. ascl:1211.002

Israelian G., Delgado Mena E., Santos N. C., Sousa S. G., Mayor M., Udry S., Domínguez Cerdeña C., et al., 2009, Natur, 462, 189. doi:10.1038/nature08483

Jackson B., Barnes R., Greenberg R., 2009, ApJ, 698, 1357. doi:10.1088/0004-637X/698/2/1357

Jackson B., Adams E. R., Morgenthaler J. P., 2023, AJ, 166, 142. doi:10.3847/1538-3881/acef00

Jia S., Spruit H. C., 2017, MNRAS, 465, 149

Jia S., Spruit H. C., 2018, MNRAS, 864, 169

Joyce M., Tayar J., 2023, Galaxies, 11, 75. doi:10.3390/galaxies11030075

Kane S. R., 2023, ApJ, 958, 120. doi:10.3847/1538-4357/ad06b2

Kashi A., Michaelis A. M., Feigin L., 2019, Galax, 8, 2. doi:10.3390/galaxies8010002

Kippenhahn R., Ruschenplatt G., Thomas H.-C., 1980, A&A, 91, 175

Kunitomo M., Guillot T., Buldgen G., 2022, A&A, 667, L2. doi:10.1051/0004-6361/202244169

Kunitomo M., Buldgen G., Guillot T., 2025, A&A, 702, A167. doi:10.1051/0004-6361/202555104

Kunz R., Fey M., Jaeger M., Mayer A., Hammer J. W., Staudt G., Harissopulos S., et al., 2002, ApJ, 567, 643. doi:10.1086/338384

Lane K., Stephan A., Soares-Furtado M., Stassun K., Yarza R., 2025, DDA, 56, 204.12

Lau M. Y. M., Cantiello M., Jermyn A. S., MacLeod M., Mandel I., Price

D. J., 2025, A&A, 694, A264. doi:10.1051/0004-6361/202452081
Lazovik Y. A., 2023, MNRAS, 520, 3749. doi:10.1093/mnras/stad394
Liddle A. R., 2007, MNRAS, 377, L74
Ludwig H.-G., Freytag B., Steffen M., 1999, A&A, 346, 111. doi:10.48550/arXiv.astro-ph/9811179
MacLeod, M., & Ramirez-Ruiz, E. 2015, ApJ, 803, 41
Magg E., Bergemann M., Serenelli A., Bautista M., Plez B., Heiter U., Gerber J. M., et al., 2022, A&A, 661, A140. doi:10.1051/0004-6361/202142971
Martin R. G., Livio M., 2016, ApJ, 822, 90. doi:10.3847/0004-637X/822/2/90
Meléndez J., Asplund M., Gustafsson B., Yong D., 2009, ApJL, 704, L66. doi:10.1088/0004-637X/704/1/L66
Metzger B. D., Giannios D., Spiegel D. S., 2012, MNRAS, 425, 2778
Montalbán J., Miglio A., Noels A., Grevesse N., di Mauro M. P., 2004, ESASP, 559, 574. doi:10.48550/arXiv.astro-ph/0408055
Morgan, J. V., Bralower, T. J., Brugger, J. & Wünnemann, K. The Chicxulub impact and its environmental consequences, Nat. Rev. Earth & Environ. 3, 338, DOI: 10.1038/s43017-022-00283-y (2022)
Mustill, A. J., & Villaver, E. 2012, ApJ, 761, 121
Nagar T., Spina L., Karakas A. I., 2020, ApJL, 888, L9. doi:10.3847/2041-8213/ab5dc6
Nguyen C. T., Bressan A., Korn A. J., Cescutti G., Costa G., Addari F., Girardi L., et al., 2025, A&A, 696, A136. doi:10.1051/0004-6361/202451847
Nordlund Å., 2025, arXiv, arXiv:2506.04199. doi:10.48550/arXiv.2506.04199
Ocampo M. M., Miller Bertolami M. M., Córsico A. H., Althaus L. G., 2025, arXiv, arXiv:2512.04900. doi:10.48550/arXiv.2512.04900
O'Connor C. E., Bildsten L., Cantiello M., Lai D., 2023, ApJ, 950, 128. doi:10.3847/1538-4357/acd2d4
Oetjens A., Carone L., Bergemann M., Serenelli A., 2020, A&A, 643, A34. doi:10.1051/0004-6361/202038653
Ong J. M. J., Hon M. T. Y., Soares-Furtado M., Stephan A. P., van Saders J., Tayar J., Shappee B., et al., 2024, ApJ, 966, 42. doi:10.3847/1538-4357/ad2ea2
Paquette C., Pelletier C., Fontaine G., Michaud G., 1986, ApJS, 61, 197. doi:10.1086/191112
Paxton B., Bildsten L., Dotter A., Herwig F., Lesaffre P., Timmes F., 2011, ApJS, 192, 3. doi:10.1088/0067-0049/192/1/3
Rao S., Pezzotti C., Meynet G., Eggenberger P., Buldgen G., Mordasini C., Bourrier V., et al., 2021, A&A, 651, A50. doi:10.1051/0004-6361/202039965
Ray T. P., Ferreira J., 2021, NewAR, 93, 101615. doi:10.1016/j.newar.2021.101615
Retter A., Zhang B., Siess L., Levinson A., 2006, MNRAS, 370, 1573. doi:10.1111/j.1365-2966.2006.10585.x
Richer J., Michaud G., Turcotte S., 2000, ApJ, 529, 338. doi:10.1086/308274
Rilinger A. M., Espaillat C. C., Xin Z., Ribas Á., Macías E., Luettgen S., 2023, ApJ, 944, 66. doi:10.3847/1538-4357/aca905
Rogers F. J., Nayfonov A., 2002, ApJ, 576, 1064. doi:10.1086/341894
Ronco M. P., Schreiber M. R., Giuppone C. A., Veras D., Cuadra J., Guilera O. M., 2020, ApJL, 898, L23. doi:10.3847/2041-8213/aba35f
Ryabchikova T., Pakhomov Y., Mashonkina L., Sitnova T., 2022, MNRAS, 514, 4958. doi:10.1093/mnras/stac1675
Ryan S. G., 2000, MNRAS, 316, L35. doi:10.1046/j.1365-8711.2000.03777.x
Sandquist E. L., Dokter J. J., Lin D. N. C., Mardling R. A., 2002, ApJ, 572, 1012
Schwarz G., 1978, Ann. Statist., 6, 461
Seaton M. J., 2005, MNRAS, 362, L1. doi:10.1111/j.1365-2966.2005.00019.x
Serenelli A. M., Haxton W. C., Peña-Garay C., 2011, ApJ, 743, 24. doi:10.1088/0004-637X/743/1/24
Siess, L., & Livio, M. 1999, MNRAS, 308, 1133
Soares B. M. T. B., Adibekyan V., Mordasini C., Deal M., Sousa S. G., Delgado-Mena E., Santos N. C., et al., 2025, A&A, 693, A47. doi:10.1051/0004-6361/202451399
Southworth J., 2011, MNRAS, 417, 2166. doi:10.1111/j.1365-2966.2011.19399.x
Spina L., Palla F., Randich S., Sacco G., Jeffries R., Magrini L., Franciosini E., et al., 2015, A&A, 582, L6. doi:10.1051/0004-6361/201526896
Spina L., Sharma P., Meléndez J., Bedell M., Casey A. R., Carlos M., Franciosini E., et al., 2021, NatAs, 5, 1163. doi:10.1038/s41550-021-01451-8
Staff, J. E., De Marco, O., Wood, P. R., Galaviz, P., Passy, J.-C., & Iaconi, R. 2016,MNRAS, 458, 832
Sun Q., Wang S. X., Gan T., Ji C., Lin Z., Ting Y.-S., Teske J., et al., 2025, ApJ, 980, 179. doi:10.3847/1538-4357/ad9924
Tayler R. J., 1986, MNRAS, 220, 793. doi:10.1093/mnras/220.4.793
Théado, S., & Vauclair, S. 2012, ApJ, 744, 123
Thoul A. A., Bahcall J. N., Loeb A., 1994, ApJ, 421, 828. doi:10.1086/173695
Ulrich R. K., 1972, ApJ, 172, 165. doi:10.1086/151336
Vissapragada S., Chontos A., Greklek-McKeon M., Knutson H. A., Dai F., Pérez González J., Grunblatt S., et al., 2022, ApJL, 941, L31. doi:10.3847/2041-8213/aca47e
Winnick I., Yana Galarza J., Reggiani H., Ferreira T., Baraffe I., Lorenzo-Oliveira D., Oyague M., et al., 2025, arXiv, arXiv:2508.16513. doi:10.48550/arXiv.2508.16513
Yana Galarza J., Reggiani H., Ferreira T., Lorenzo-Oliveira D., Simon J. D., McWilliam A., Schlaufman K. C., et al., 2024, ApJ, 974, 122. doi:10.3847/1538-4357/ad697f
Yarza R., MacLeod M., Loeb A., Guillochon J., 2023, ApJ, 949, 18
Yee S. W., Winn J. N., Knutson H. A., Patra K. C., Vissapragada S., Zhang M. M., Holman M. J., et al., 2020, ApJL, 888, L5. doi:10.3847/2041-8213/ab5c16
Yıldız M., Kızıloğlu N., 1997, A&A, 326, 187. doi:10.48550/arXiv.astro-ph/9706228
Yıldız M., Yakut K., Bakış H., Noels A., 2006, MNRAS, 368, 1941. doi:10.1111/j.1365-2966.2006.10275.x
Yıldız M., 2007, MNRAS, 374, 1264. doi:10.1111/j.1365-2966.2006.11218.x
Yıldız M., 2008, MNRAS, 388, 1143. doi:10.1111/j.1365-2966.2008.13352.x
Yıldız M., 2011, MNRAS, 412, 2571. doi:10.1111/j.1365-2966.2010.18075.x
Yıldız M., Çelik Orhan Z., Aksoy Ç., Ok S., 2014, MNRAS, 441, 2148. doi:10.1093/mnras/stu662
Yıldız M., Çelik Orhan Z., Kayhan C., 2015, MNRAS, 448, 3689. doi:10.1093/mnras/stv295
Yıldız M., 2015, RAA, 15, 2244. doi:10.1088/1674-4527/15/12/012
Yıldız M., Çelik Orhan Z., Örtel S., Çakır T., 2024, MNRAS, 528, 6881. doi:10.1093/mnras/stae476
Yun S., Lee Y. S., Kim Y. K., Beers T. C., Togay B., Lim D., 2024, ApJ, 971, 35. doi:10.3847/1538-4357/ad5722
Zhang Q.-S., Li Y., Christensen-Dalsgaard J., 2019, ApJ, 881, 103. doi:10.3847/1538-4357/ab2f77

This paper has been typeset from a TEX/LATEX file prepared by the author.